TOPICAL REVIEW

Dislocations in 4H silicon carbide

To cite this article: Jiajun Li *et al* 2022 *J. Phys. D: Appl. Phys.* **55** 463001

View the article online for updates and enhancements.

Topical Review

Dislocations in 4H silicon carbide

Jiajun Li[1,2]**, Guang Yang**[3]**, Xiaoshuang Liu**[1,2,4]**, Hao Luo**[1,2]**, Lingbo Xu**[3] **,
Yiqiang Zhang**[5] **, Can Cui**[3] **, Xiaodong Pi**[1,2,*] **, Deren Yang**[1,2] **and Rong Wang**[1,2,*]

[1] State Key Laboratory of Silicon Materials and School of Materials Science and Engineering, Zhejiang
University, Hangzhou 310027, People's Republic of China
[2] Institute of Advanced Semiconductors and Zhejiang Provincial Key Laboratory of Power
Semiconductor Materials and Devices, Hangzhou Innovation Center, Zhejiang University, Hangzhou
311200, People's Republic of China
[3] Key Laboratory of Optical Field Manipulation of Zhejiang Province, Department of Physics, Zhejiang
Sci-Tech University, Hangzhou 310018, People's Republic of China
[4] Zhejiang Province Key Laboratory of Quantum Technology and Device, Department of Physics,
Zhejiang University, Hangzhou 310027, People's Republic of China
[5] School of Materials Science and Engineering & College of Chemistry, Zhengzhou University,
Zhengzhou 450001, People's Republic of China

E-mail: xdpi@zju.edu.cn and rong_wang@zju.edu.cn

CrossMark

Abstract

Owing to the superior properties of the wide bandgap, high carrier mobility, high thermal
conductivity and high stability, 4H silicon carbide (4H-SiC) holds great promise for applications
in electrical vehicles, 5G communications, and new-energy systems. Although the
industrialization of 150 mm 4H-SiC substrates and epitaxial layers has been successfully
achieved, the existence of a high density of dislocations is one of the most severe bottlenecks for
advancing the performance and reliability of 4H-SiC based high-power and high-frequency
electronics. In this topical review, the classification and basic properties of dislocations in
4H-SiC are introduced. The generation, evolution, and annihilation of dislocations during the
single-crystal growth of 4H-SiC boules, the processing of 4H-SiC wafers, as well as the
homoepitaxy of 4H-SiC layers are systematically reviewed. The characterization and
discrimination of dislocations in 4H-SiC are presented. The effect of dislocations on the
electronic and optical properties of 4H-SiC wafers and epitaxial layers, as well as the role of
dislocations on the performance and reliability of 4H-SiC based power devices are finally
presented. This topical review provides insight into the fundamentals and evolution of
dislocations in 4H-SiC, and is expected to provide inspiration for further control of dislocations
in 4H-SiC.

Keywords: 4H-SiC, dislocations, single crystals, epitaxial layers

(Some figures may appear in colour only in the online journal)

1. Introduction

4H silicon carbide (4H-SiC) is undergoing rapid development
in the field of high-power and high-frequency electronics,
as well as the quantum information technologies, owing to
its wide bandgap, high carrier mobility, high thermal con-
ductivity and high stability [1–3]. 4H-SiC is one of the most
mature, most large-scale developed wide-bandgap semicon-
ductors. The 4H-SiC single crystals can be grown by top
seeded solution growth (TSSG), high temperature chemical
vapor deposition (HTCVD), and physical vapor transport

(PVT) approaches [4], among which the well-developed PVT technology prevails over other growth technologies because of its high maturity, sensitive temperature tunability, and low cost of the solid raw materials.

After decades of development, the commercialized 150 mm 4H-SiC single-crystal substrates are flourishing in the applications of high-power electronics based on the homoepitaxy of 4H-SiC thin films [5–7]. However, the density of dislocations in commercialized 150 mm 4H-SiC substrates is still as high as 10^3–10^4 cm^{-2} [5, 8, 9]. The high-density dislocations would either propagate into epitaxial layers, or convert to other types of dislocations or stacking faults (SFs) during the homoepitaxy of 4H-SiC. Dislocations are also found to evolve during the preparation and application of 4H-SiC based devices [10–14]. It has been found that dislocations in 4H-SiC epitaxial layers act as carrier-recombination centers, which reduce the minority carrier lifetime, increase the leakage current, and cause reliability issue of 4H-SiC based electronic devices [15]. Therefore, dislocations are one of the most severe bottlenecks stunting the applications of 4H-SiC. Understanding the basic properties of dislocations and clarifying the generation and evolution of dislocations during the single-crystal growth, substrate wafering and homoepitaxy of 4H-SiC are critical to tailoring the dislocation configuration, reducing the dislocation density and tuning the properties of dislocations in 4H-SiC.

In this topical review, we discuss the recent progress related to dislocations in 4H-SiC. Firstly, we introduce the basic properties of dislocations in 4H-SiC. We then discuss the generation and evolution of dislocations during the single-crystal growth and substrate wafering of 4H-SiC. The propagation and conversion of dislocations during the homoepitaxy of 4H-SiC are then presented. Finally, the summary and future prospects for controlling dislocations in 4H-SiC are described.

2. Basic properties of dislocations in 4H-SiC

The basic structures of the 4H-SiC lattice and dislocations are shown in figure 1 [16]. Figure 1(a) schematically displays the hexagonal unit cell and fundamental translation vectors of 4H-SiC. The basis translation vectors along the axial and basal directions are defined as c and a, respectively. In hexagonal 4H-SiC, dislocations are classified into threading dislocations (TDs) and basal plane dislocations (BPDs). The Burgers vectors, dislocation-line directions and densities of dislocations in commercialized 150 mm 4H-SiC single-crystal substrates are summarized in table 1 [5, 8, 9]. TDs in 4H-SiC can be classified into micropipes (MPs), threading screw dislocations (TSDs), threading mixed dislocations (TMDs) and threading edge dislocations (TEDs), which have the Burgers vectors of $\pm n\bm{c}$ (n = 3–10), $\pm \bm{c}$, $\bm{c} + \bm{a}$, and $([11\bar{2}0]/3)\,\bm{a}$, respectively [17]. An elementary TSD in 4H-SiC is located at the center of a spiral with a four-bilayer-height step (ABCD in figure 1(b)), corresponding to |1$\bm{c}$|. Slipping along $[11\bar{2}0]/3$ results in an extra (or missing) half plane with two types of dislocations, i.e. a BPD lying in the basal plane (line AB) and a TED along

the [0001] direction (line BC) (figure 1(c)). Because of the Peierls potential, BPDs tend to lie along the $[11\bar{2}0]$ direction (line A'B) instead of the pure edge type with dislocation line along $[11\bar{2}0]/3$ (figure 1(d)).

A BPD is prone to dissociate into two partial dislocations (PDs), $([10\bar{1}0]/3)\,\bm{a}$ and $([01\bar{1}0]/3)\,\bm{a}$, that are separated by a single Shockley-type SF (SSF) on the basal plane of 4H-SiC [18–20]. According to the core species, the PDs can be classified into the Si-core PD and C-core PD, of which the Si-core PD is easier to be activated to glide under the UV illumination, electron irradiation and the electron–hole recombination [21–23].

Dislocations in 4H-SiC substrates can be generated during the growth and wafering processes as well as be replicated from seeds [24, 25], many efforts have been made to reduce the dislocations densities. Up to now, the density of device-killing MPs decreases to be lowered than 0.1 cm^{-2} in 4H-SiC substrates, while the densities of the other dislocations remain in the orders of magnitude of 10^2–10^4 cm^{-2} [5, 8, 9].

3. Generation of dislocations during the single-crystal growth of 4H-SiC

3.1. Generation of dislocations

During the PVT growth of 4H-SiC single crystals, dislocations are generated under either thermal stress because of the radial temperature gradient, or steric stress around secondary phases and 2D islands. Most TDs are generated in the initial growth stage of 4H-SiC single crystals, which is confirmed by synchrotron x-ray topography (XRT) technologies [26, 27]. TDs in the seed crystal tend to propagate along the growth direction of a 4H-SiC single crystal, and give rise to the inheritance of TDs from the 4H-SiC seed crystal to the 4H-SiC boule. Figure 2(a) displays the transmission XRT image of a 4H-SiC single crystal in the initial stage of crystal growth, where the dark line-shaped contrasts correspond to TSDs propagating from the seed crystal to the grown crystal [28]. The abnormal nucleation would occur at the surface of the seed crystal, as a result of growth condition discontinuities, such as the discontinuities of temperature-distribution, C/Si ratio, and doping concentrations. The abnormal nucleation gives rise to the orientation mismatch, and thus the nucleation of TDs [29–31]. The TSD pairs caused by the mismatch can be found in the early stage of PVT growth of 4H-SiC crystal [32], which is evidenced by a mesa caused by the two opposite spirals of the closely spaced TSDs on the surface (figure 2(b)) [33]. As the PVT growth proceeds, the generation of MPs is found around the secondary phases, such as polytypes, carbon inclusions, and voids (figure 2(c)) [33]. With the development of the growth technologies, the secondary phases have been well controlled, which yields 'zero-MP' 4H-SiC single crystals [34, 35]. Since the seed inheritance and TD generation in the initial stage are key to the TD generation, Nakamura *et al* invented the repeated *a*-face growth (RAF)
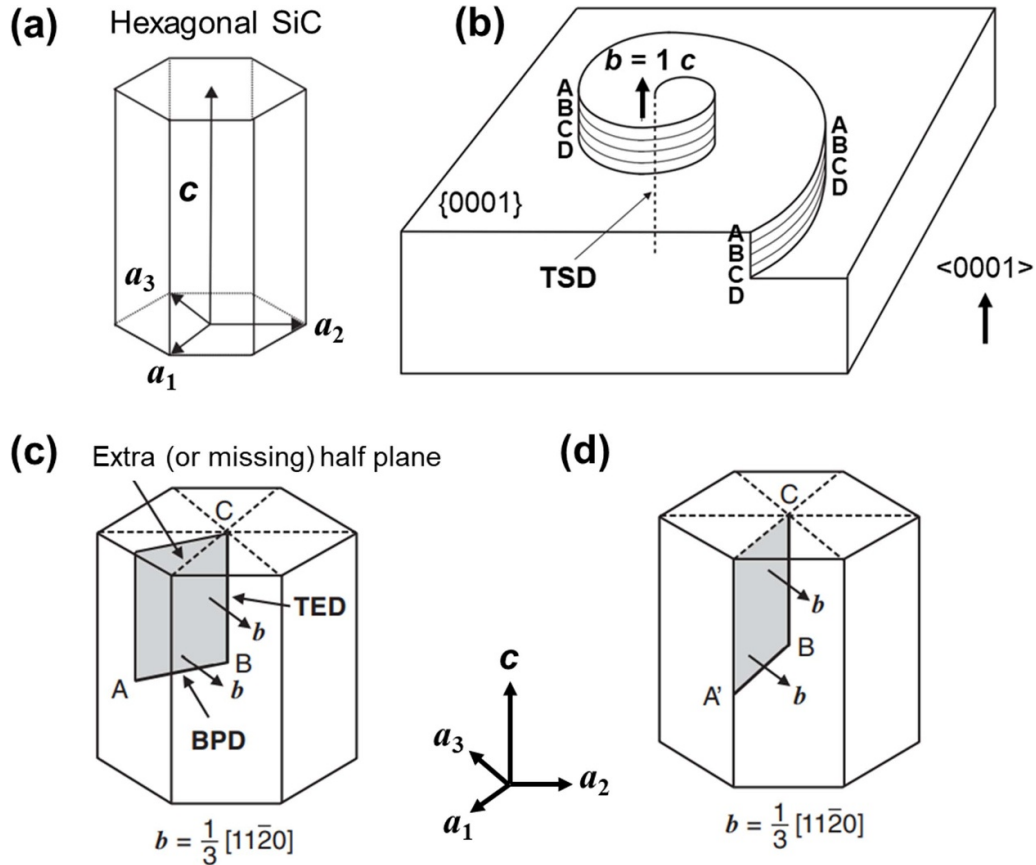
Figure 1. (a) Hexagonal unit cell and fundamental translation vectors a and c of 4H-SiC. (b) Schematic illustration of an elementary TSD in 4H-SiC, which is located at the center of a spiral with a four-bilayer-height step, represented by ABCD. (c) Schematic illustration of an extra (or missing) half plane in a 4H-SiC crystal. The dislocation along line AB (basal plane) is a BPD while that along line BC ([0001] direction) is a TED. (d) Typical configuration of TEDs and BPDs, where the BPD line is along a $\langle 11\bar{2}0 \rangle$ direction. (a)–(d) [16] John Wiley & Sons. © 2014 John Wiley & Sons Singapore Pte. Ltd.

Table 1. Burgers vectors, dislocation-line directions and dislocation densities of TDs and BPDs in commercialized 150 mm 4H-SiC single crystals [5, 8, 9].

	Dislocations	Burgers vector	Dislocation-line direction	Density (cm^{-2})
TDs	Micropipe (MP)	nc ($n = 3$–10)	[0001]	<0.1
	Threading screw dislocation (TSD)	c	[0001]	10^2–10^3
	Threading mixed dislocation (TMD)	$c + a$	[0001]	
	Threading edge dislocation (TED)	$([11\bar{2}0]/3)\,a$	[0001]	10^3–10^4
BPDs	Integrated basal plane dislocation (BPD)	$([11\bar{2}0]/3)\,a$	In (0001) plane (predominantly along [$11\bar{2}0$])	10^2–10^4
	Decomposed BPD	$([10\bar{1}0]/3)\,a + ([01\bar{1}0]/3)\,a$	In (0001) plane	

process, which reduces the density of dislocations in 4H-SiC [36].

The generation of BPDs is similar to that of TDs. BPDs can also be inherited from the seed crystal, due to the off-axis slicing of the 4H-SiC seed crystals. It has been found that the density of BPDs in the middle and top of the 4H-SiC boule (that is, away from the seed crystal) is higher than that at the bottom of the boule (that is, near the seed crystal), indicating that high-density BPDs are generated at

the middle and late growth stages [37]. This means that the thermal stress, rather than inheritance from the seed crystal, dominates the generation of BPDs during the single-crystal growth of 4H-SiC. Numerical simulations were carried out to understand the nucleation and distribution of BPDs during the single-crystal growth of 4H-SiC. Gao and Kakimoto used the Alexander–Haasen model to simulate the plastic deformation of 4H-SiC during the single-crystal growth of 4H-SiC [38], and found that the large radial-temperature gradient near the
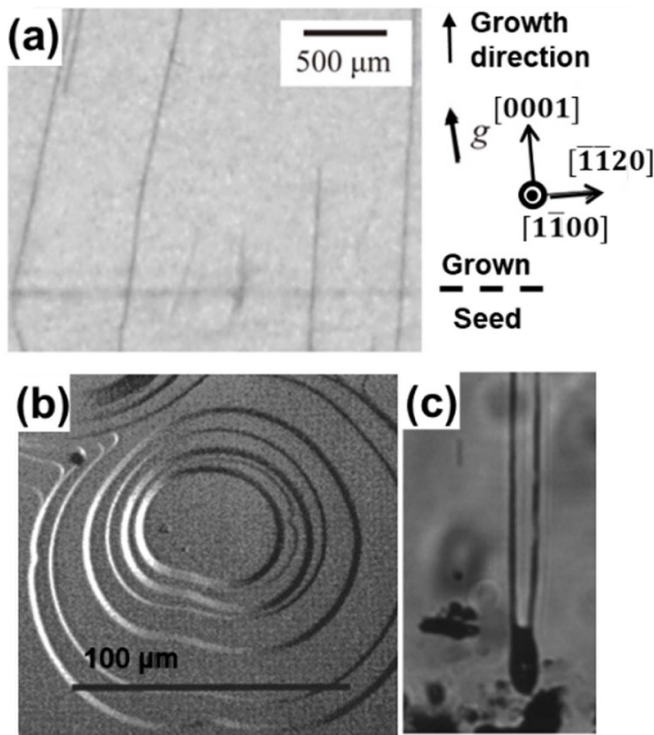
Figure 2. (a) Transmission XRT images with 0004 diffraction of 4H-SiC crystal at the initial stage of the crystal growth. The line-shape contrasts denote TSDs generated in the initial growth stage, and the horizontal dark contrast at the interface of seed and grown crystal is attributed to the anomalous diffraction of the local lattice strain. Reproduced from [28]. © 2018 The Japan Society of Applied Physics. All rights reserved. (b) Atomic force microscope (AFM) image showing a typical mesa morphology showing two opposite spirals of a TSD pair on the growth face of a 4H-SiC crystal. (c) Nucleation of a pair of MPs from a small isolated inclusion in 4H-SiC. (b) and (c) Reprinted from [33], with the permission of AIP Publishing.

crystal edge is the main reason for the high dislocation density in this region (figure 3(a)). Therefore, reducing the heating flux near the crystal edge would reduce the dislocation density in 4H-SiC single crystals. Besides, increasing the cooling time was found to be beneficial for the reduction of the total dislocation density in 4H-SiC single crystals (figure 3(b)). The critical shear stress for the nucleation of BPDs during PVT growth is about 1 MPa at 2200 °C. When the thermoelastic stress in the crystal exceeds the critical shear stress, BPDs begin to nucleate and multiply during the single-crystal growth [39–42]. However, the Alexander–Haasen model cannot distinguish BPDs from TDs in 4H-SiC [43–45]. Because the shear stress plays the dominant role in the nucleation of BPDs, Gao and Kakimoto improved the model by firstly resolving the thermal stress in the primary slip direction and then substituting the resolved shear stress into the three-dimensional Alexander–Haasen model to obtain the distribution of BPDs in 4H-SiC [46]. The distributions of BPDs inside a 4H-SiC single crystal with different growth times and cooling times are shown in figures 3(c) and (d), respectively. Clearly, the density of BPDs in 4H-SiC single crystals increases with increasing growth time, which is attributed to the large thermal stress

caused by the gradually increased convexity. Meanwhile, the cooling time also exerts significant effect on the density of BPDs in 4H-SiC. The density of BPDs in a 4H-SiC boule with the cooling time of 1 h is much lower than that in a 4H-SiC boule with the cooling time of 10 h, which is caused by the smaller radial heating flux between the boule and the crucible during the cooling process with less cooling time. Therefore, increasing the cooling rate is also beneficial for the reduction of BPD density in 4H-SiC single crystals, which has been verified by experimental research [47].

Besides inheritance from the seed and generation by the thermoelastic stress, the nucleation region also plays an important role in the generation and multiplication of BPDs. According to the surface morphologies, the growth front of a 4H-SiC boule can be divided into the facet region, non-facet region, and the intermediate region between them (figure 4(a)) [48]. The formation kinetics of dislocations is different in these regions. XRT observations revealed that BPDs are nucleated in the shoulder region of the growth front, which may originate from the shear stresses on the convex growth front. BPDs are rarely introduced in the facet and near-facet regions of the grown boule [48]. The dislocation lines of BPDs are terminated when they extend to the facet and near-facet regions, which reduces the BPD density and even creates BPD-free region beneath these regions, as illustrated in figure 4(b). The physical model is also supported by Raman measurements, as shown in figure 4(c). Raman spectra along the growth direction indicate that the peak position of the E_2 mode shifts abruptly where bunched BPDs existed, indicating that the bunched BPDs are introduced at the domed surface and are hardly introduced from the side surfaces of the grown crystals [49]. The most plausible location where BPDs are introduced would be the shoulder regions of growth crystals.

3.2. Evolution of dislocations during the single-crystal growth

3.2.1. Conversion between MPs and TSDs.
MPs are device-killing defects in 4H-SiC. It has been found that the open-core MPs can be either inherited from the seed crystal or directly generated from mesoscopic inclusions, such as carbon inclusions, silicon droplets, and polytype disturbances (figures 5(a)–(d)) [33, 50, 51]. The Burgers vectors of MPs and TSDs are nc ($n = 3–10$) and c, respectively. According to Frank's theory, when the Burgers vector of a spiral TSD or a TMD exceeds $3c$, the open-core MP is formed as a result of energy minimization so that the contribution of the surface energy of the MP wall is smaller than the energy associated with filling the MP [52]. This indicates that the multiplication of the closed-core TSDs would give rise to the formation of the open-core MP (figure 5(e)) [16, 53, 54]. It has been found that MPs can outcrop at TSDs with the same Burgers vectors [55]. Similarly, the filling of MPs is achieved by decomposition of a single MP to several closed-core TSDs [56, 57], which is often observed during the epitaxy of 4H-SiC thin films. By sequential KOH etching, thinning, polishing, and KOH etching, Kamata *et al* observed the transition of the etch pits from several separated pits to line-shaped pits in the epilayer, and finally to one single large pit in the substrate
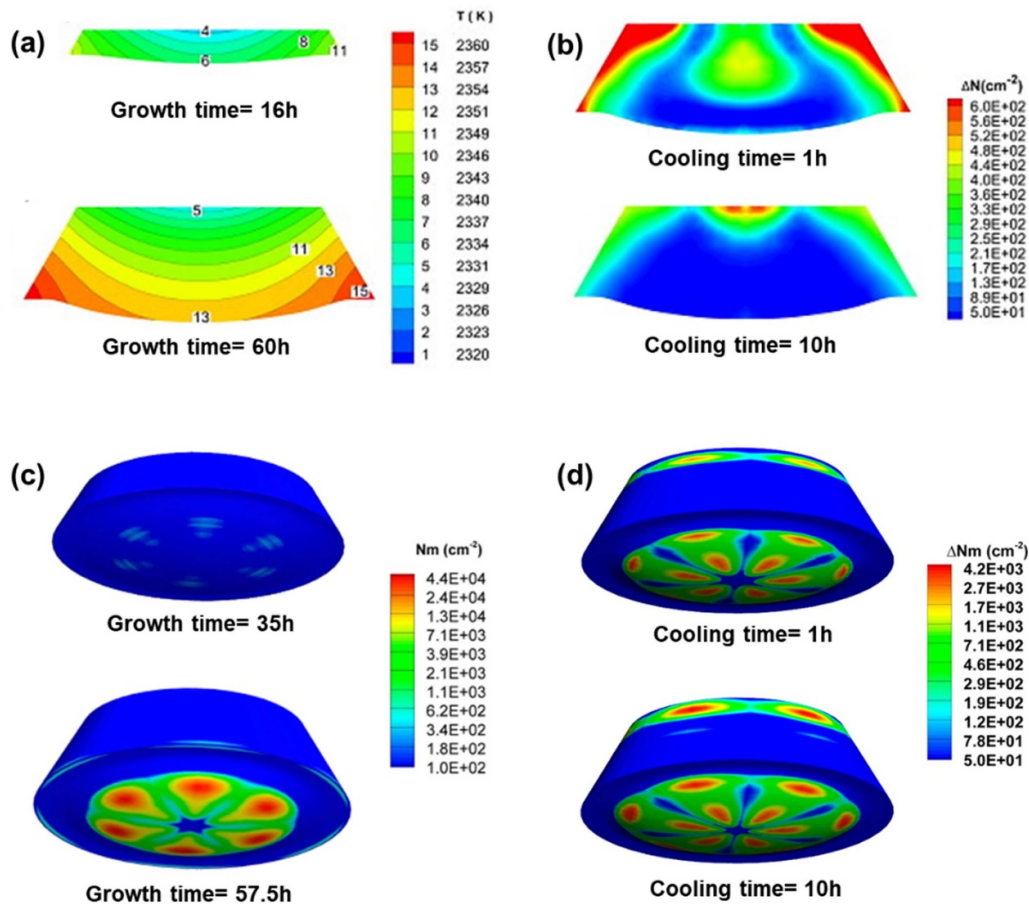
Figure 3. (a) Simulation of the temperature distribution in a 4H-SiC boule with the growth times of 16 h and 60 h, showing the large radial temperature gradient near the edge of the boule. (b) Total dislocation density (TDs + BPDs) distribution in a 4H-SiC boule with the cooling times of 1 h and 10 h. (a) and (b) Reprinted from [38], Copyright (2014), with permission from Elsevier. (c) Calculated three-dimension BPD-density distribution in a 4H-SiC boule with the growth times of 35 h and 57.5 h. (d) Calculated three-dimension BPD-density distribution in a 4H-SiC boule with cooling times of 1 h and 10 h. (c) and (d) Reprinted with permission from [46]. Copyright (2014) American Chemical Society.

with the etching-polishing process, which indicates that the MP is converted to TSDs during the homoepitaxy of 4H-SiC (figures 5(f) and (g)) [58, 59].

3.2.2. Conversion of TSDs to SFs. During the single-crystal growth of 4H-SiC, TSDs can be converted to Frank-type SFs via the macrosteps [60–62]. As shown in figures 6(a) and (b), a TSD in the seed crystal was found to convert to a Frank-type SF during the TSSG growth of 4H-SiC single crystals [63, 64]. With the macrostep-assisted conversion mechanism, the difference in the length of the converted SFs (C' in figure 6(b)) indicates that the conversion of TSDs continuously happens as the single-crystal growth proceeds, with the macrostep-assisted transition mechanism being depicted in figure 6(c). SFs then propagate laterally toward the edge of the crystal and terminated at the surface finally. The surface polarity exerts significant effect on the conversion of TSDs. During the TSSG growth of 4H-SiC single crystals on off-axis seed crystals, the conversion of TSDs only occurs for growth on (0001) Si-face of the seed crystal [63]. The macrostep-assisted conversion of TSDs to Frank-type SFs is also observed in PVT-grown

4H-SiC single crystals, indicating the overgrowth of vicinal macrosteps causes the reorientation, and thus the conversion of TSDs [65]. TSDs and TMDs are also found to convert to complicated basal plane defects containing both Frank-type SFs and Shockley-type SFs. Figures 6(d) and (e) display the synchrotron white beam x-ray topographic (SWBXT) images on $\{01\bar{1}0\}$ and $\{0\bar{1}11\}$ reflections, respectively [66]. The conversion area consists of SF A and SF B. The SF A shows strong contrast on $\{01\bar{1}0\}$ reflections and weak contrast on $\{0\bar{1}11\}$ reflections, while SF B shows strong contrast only on $\{0\bar{1}11\}$ reflections. Detailed analysis indicated that the fault vectors of SFs A and B are $1/6\langle20\bar{2}3\rangle$ and $1/2[0001]$, respectively. The conversion mechanism is shown in figure 6(f). The surface outcrop of a pure TSD leads to the generation of two $c/2$-high demisteps (Frank partial) separated by a $c/2$ Frank-type SF with the macrostep overgrowth. It is further divided into two SFs when the macrostep front grows over the dislocation with the Burgers vector of $c + a$ dislocation ($c + a$ dislocation, CPAD), which gives rise to the formation of SF B. In addition, the conversion of a dislocation with the Burgers vector of $c + a$ can also happen by the macrostep overgrowth. The spiral component c develops into the sessile
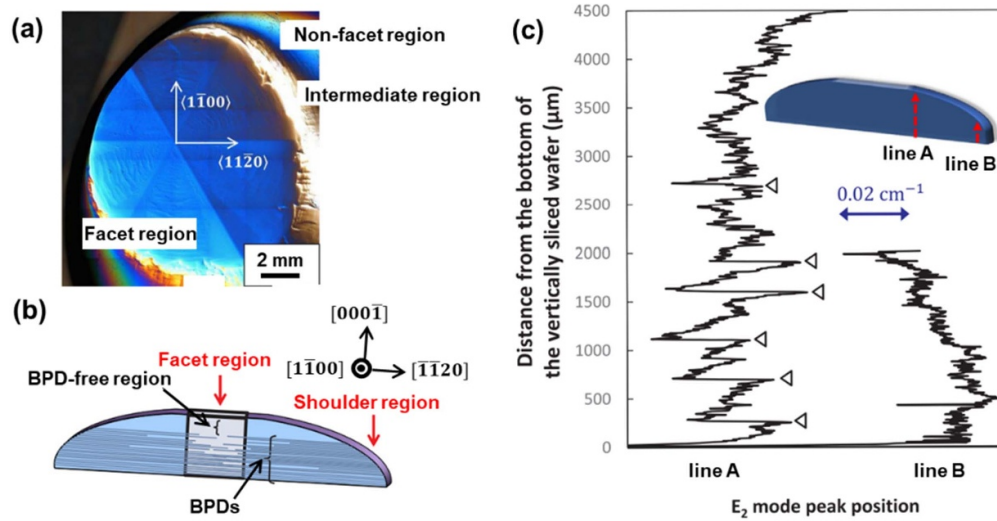
J. Phys. D: Appl. Phys. **55** (2022) 463001

Topical Review

Figure 4. (a) Differential interference contrast (DIC) optical microscope image of the growth front of a 4H-SiC boule. The growth front of the C face of a 4H-SiC boule consists of three regions, that is, the facet region, the non-facet region and the intermediate region. (b) Schematic diagram illustrating the distribution of BPDs in a PVT-grown 4H-SiC boule. BPDs extend from the shoulder region of the growth front and are terminated in the region beneath the facet. The top portion beneath the facet and near facet region is almost BPD-free. (a) and (b) Reprinted from [48], Copyright (2018), with permission from Elsevier. (c) Variation of the peak positions of the E_2 mode along the growth direction of a 4H-SiC boule at the shoulder region near the facet (line A) and that near the edge of the boule (line B). The abrupt shifts are denoted by open triangles. Reprinted from [49], Copyright (2019), with permission from Elsevier.
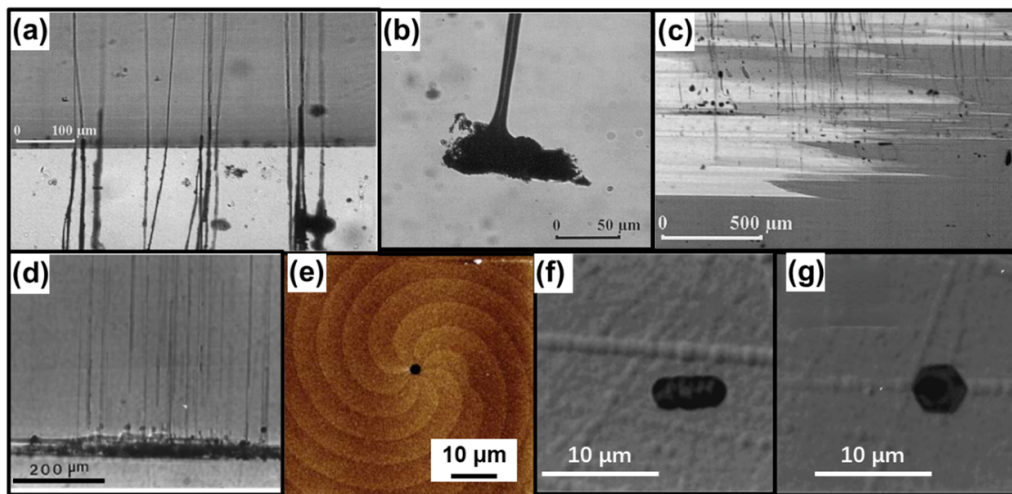

Figure 5. (a) MPs in the 4H-SiC seed crystal penetrate into the grown crystal. The lighte and darke region are the seed crystal and grown crystal, respectively. (b) A MP generated from a carbon inclusion during the growth process. (c) The formation of a multitude of MPs at the polytype disturbances. (a)–(c) Reprinted from [51], Copyright (2005), with permission from Elsevier. (d) Generation of MPs at a group of inclusions in 4H-SiC. Reprinted from [33], with the permission of AIP Publishing. (e) AFM image showing the generation of an open-core MP in the center of a TSD spiral. [16]. John Wiley & Sons. © 2014 John Wiley & Sons Singapore Pte. Ltd. (f) Four contiguous etch pits of TSDs on the 4H-SiC epitaxial layer after KOH etching. (g) The etch pit of a MP in the 4H-SiC substrate, taken from the same place as (f) after the etching-polishing process. (f) and (g) Reproduced from [58]. © 2000 The Japan Society of Applied Physics. All rights reserved.

Shockley SF (Shockley partial) and the edge component **a** develops into the glissile SF (Shockley partial), resulting in the formation of SF A [66]. The configurations are attributed to the macrostep-overgrowth assisted combined deflection of the surface outcrops of TSDs and TMDs [66, 67]. After the conversion, the lateral SFs tend to propagate towards the boundary of the single crystal, which would reduce the dislocation density of TSDs and TMDs in 4H-SiC single crystals. By

optimization of the step-flow growth and tailoring the macrostep height, Yamamoto *et al* enhanced the conversion ratio of TSDs to Frank-type SFs during the TSSG growth of 4H-SiC single crystals, and reduced the density of TSDs to 30 cm^{-2} [61]. Mitani *et al* proposed to reduce the dislocation density in 4H-SiC single crystals by firstly growing a TSD conversion layer with the solution-growth method and then growing bulk single crystals by the PVT approach. By adopting the 15° off
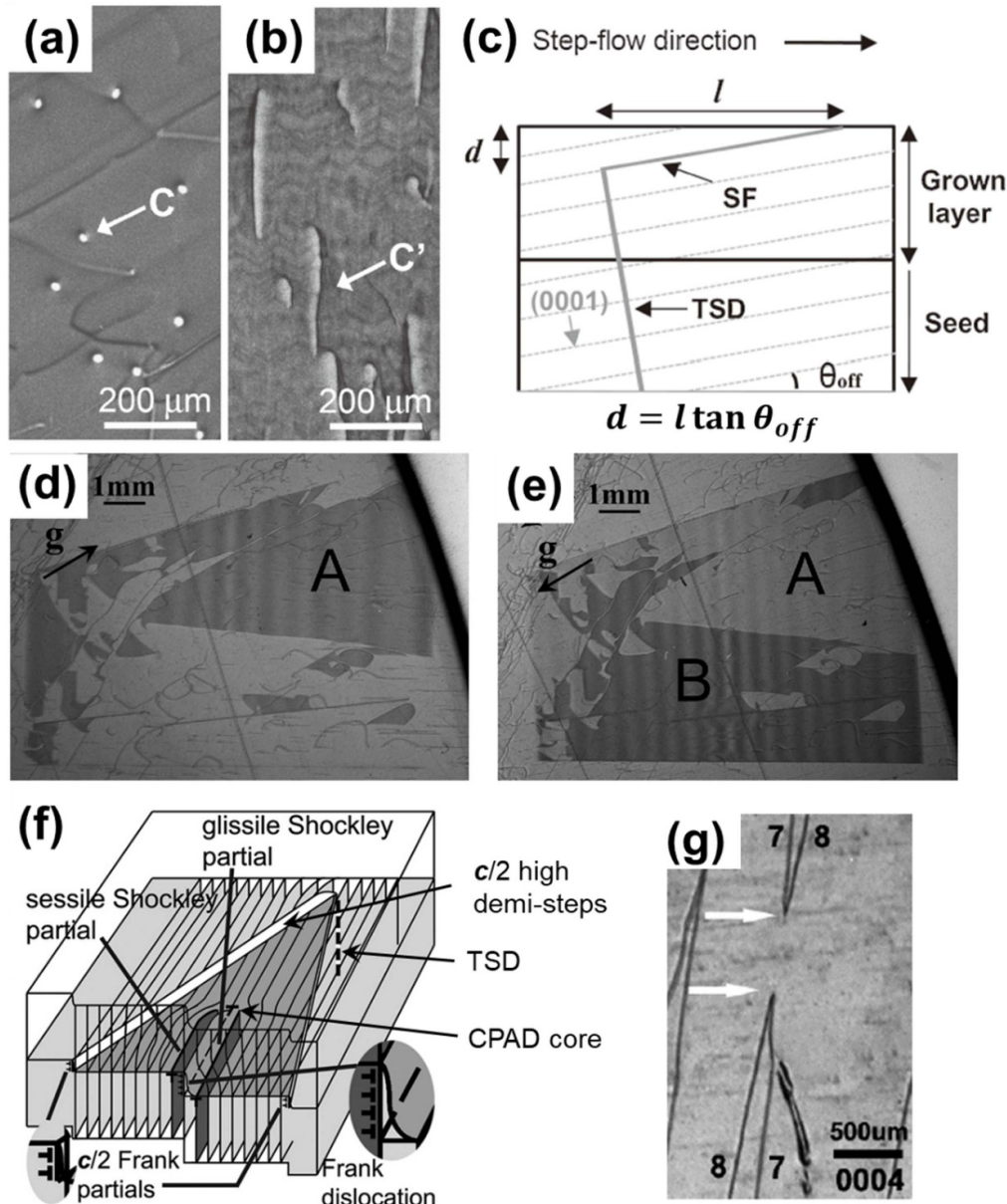
Figure 6. XRT images of the Si-face of the 4H-SiC (a) seed crystal and (b) grown crystal taken at the same position. The TSD in the seed crystal and the converted Frank-type SF in the grown crystal are marked as (C) and (C'), respectively. (c) The schematic diagram showing the conversion mechanism from a TSD to a Frank-type SF. The dislocation line of a TSD propagated into the grown crystal and converted into a SF intermittently in the growth process. The SF propagated laterally toward the boundary of the crystal and terminated at the surface finally. (a)–(c) Reproduced from [63]. © 2012 The Japan Society of Applied Physics. All rights reserved. SWBXT images on (d) $01\bar{1}0$ reflection and (e) $0\bar{1}11$ reflection recorded from a region near the edge of a 4°-offcut sliced 4H-SiC wafer. A and B are two types of SFs. (f) The conversion mechanism in (d) and (e), the macrostep front grows over a TSD first and then a dislocation with the Burgers vector of $c + a$ ($c + a$ dislocation, CPAD). (d)–(f) Reprinted from [66], with the permission of AIP Publishing. (g) XRT image ($g = 0004$) taken from a 4H-SiC wafer showing the interaction between TMDs labeled 7 and 8. Two TMDs with Burgers vectors of $-c + a$ and $c + a$, gives rise to the annihilation of the c components, leaving the a components. The annihilation points are marked with white arrows. Reproduced from [67]. © 2014 ECS—The Electrochemical Society.

seed crystals and optimizing the TSD conversion layer, TSDs are efficiently eliminated [68].

TSDs in 4H-SiC single crystals are found to be generated as TSD pairs with opposite Burgers vectors ($+c$ and $-c$) [32, 69]. As the single-crystal growth proceeds, the TSDs would interact with each other, and cause the annihilation of TSDs. Similarly, opposite-sign TSD components constituting the pair of TMDs also tend to interact with each other, which gives

rise to the evolution of the configuration of TMDs during the single-crystal growth of 4H-SiC (figure 6(g)) [67].

3.2.3. Conversion between TEDs and BPDs. Given the same Burgers vectors of the BPDs and TEDs in 4H-SiC, the mutual conversion between them occurs throughout the single-crystal growth process [70–72]. Figure 7(a) displays
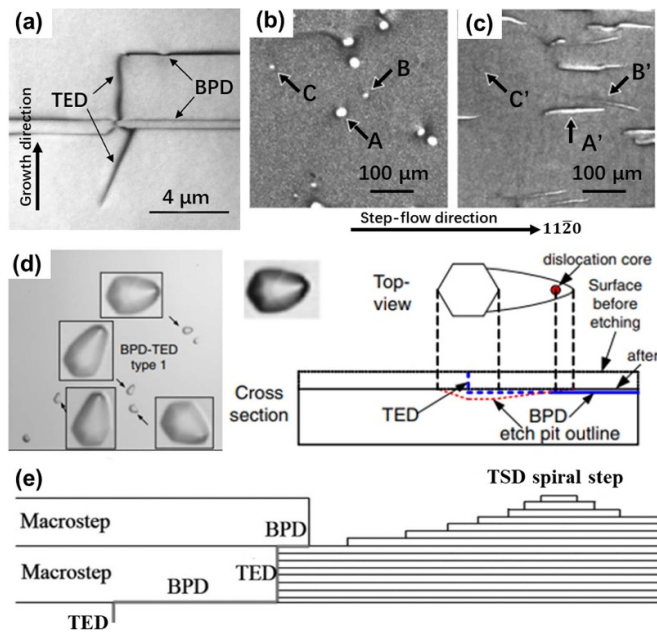
Figure 7. (a) Cross-sectional TEM image along the $[1\bar{1}00]$ zone axis showing the conversion between a BPD and a TED in 4H-SiC near the seed-grown crystal interface. Reprinted from [70], Copyright (2006), with permission from Elsevier. XRT images of the same region showing the conversion from TEDs to BPDs from the seed crystal to the grown crystal: (b) in the seed crystal, the large contrast dot A and the small contrast dots B, C correspond to a TSD and two TEDs in the seed crystal, respectively. (c) In the grown crystal, the asymmetric knife-shaped line contrast (A') and (B'), and the contrast dot (C') are the extended defects and a propagated TED in the grown 4H-SiC. The applied g vector is $11\bar{2}8$. (b) and (c) Reprinted from [71], Copyright (2014), with permission from Elsevier. (d) The morphology and formation mechanism of the BPD-TED etch pit. Reproduced from [73]. © 2011 The Japan Society of Applied Physics. All rights reserved. (e) The schematic cross-sectional diagram showing the conversion between the BPD and the TED via macrosteps. Reprinted from [75], with the permission of AIP Publishing.

the cross-sectional transmission electron microscope (TEM) image directly showing the conversion between a BPD and a TED near the seed-grown crystal interface [70]. Figures 7(b) and (c) show XRT images taken from the same region of a seed crystal and a grown crystal, respectively. Under the g vector of $11\bar{2}8$, the large point (Point A in figure 7(b)) and small point (Point B in figure 7(b)) in the seed crystal correspond to a TSD and a TED, respectively. In the grown 4H-SiC crystal, the TSD is converted to a SF (A' in figure 7(c)), and the TED is converted to a BPD (B' in figure 7(c)) [71]. The molten-alkali etching also sheds light on the conversion between BPDs and TEDs during the single crystal growth of 4H-SiC. When BPDs are converted to TEDs near the surface of the 4H-SiC substrate, the molten-alkali etching preferentially attacks the strained atoms surrounding the dislocation line of the TED, and gives rise to the formation of the hexagonal etch pit. As the etching proceeds, the isotropic etching removes the 4H-SiC layer containing the TED, and reaches the interface where the conversion from a BPD to a TED occurs during the single-crystal growth. The lateral etching along the BPD is then activated. The BPD-TED conversion near the surface gives rise to

the formation of the sea-shell shaped etch pit ending with a hexagonal etch pit (figure 7(d)) [73]. The transition from the TED to the BPD can be revealed by alternating molten-alkali etching and mechanical polishing [74]. During the step-flow growth of 4H-SiC, the growth direction can be either perpendicular growth along the axial direction of the step or the lateral growth along the direction of the step flow. The conversion between a BPD and a TED is assisted by macrosteps, and gives rise to the hopping Frank–Read manipulation of BPDs during the single-crystal growth of 4H-SiC. Starting from a TED, the surface outcrop of the TED is firstly deflected to the basal plane by the macrostep, which creates a segment of a BPD. With the advancing of the macrostep, the BPD is replicated along the direction of the step flow (figure 7(e)) [75]. When the advancing macrostep encounters another step in the opposite direction (a spiral step from a TSD is illustrated as an example), the BPD will be re-converted to the TED along the macrostep. The conversion from the TED to a BPD would happen again if the outcrop of the TED encounters another macrostep.

4. Dislocations during the processing of 4H-SiC wafers

4.1. Deformation of 4H-SiC

Starting from 4H-SiC single-crystal boules, the processing of 4H-SiC wafers includes wire sawing, lapping and chemical mechanical polishing (CMP). The latter processing step removes surface damages created in the former step [76, 77]. During the mechanical processing of 4H-SiC wafers, the deformation of 4H-SiC can be divided into five regimes: the elastic deformation, the plastic deformation, the surface cracking, the subsurface cracking, and the micro-abrasive regime [78].

Nanoindentation is widely used to investigate the deformation mechanism and mechanical properties of 4H-SiC [79, 80]. It has been found that the critical indentation depth of the elastic–plastic deformation is 23.5 nm for 4H-SiC [85]. When the indentation depth is higher than 23.5 nm, the irreversible plastic deformation gives rise to the nucleation and glide of dislocations, phase transitions, and amorphization in 4H-SiC. Molecular dynamics simulations indicate that the shear stress dominates the stress field, and gives rise to the formation of BPDs and amorphization of 4H-SiC [81]. As shown in figure 8(a), when the indentation depth is 0.5 nm, the amorphous structure is firstly formed underneath the indenter. As the indentation depth increases, the lateral deformation gives rise to the lateral extension of amorphous structures and shear loops, which leads to the expansion of the amorphous region and more lateral BPDs when indentation depth increases to 6.5 nm. By combining nanoindentation tests and TEM observations, Liu *et al* confirmed that the shear stress prevails over tensile stress in the low-load nanoindentation-induced stress field, which gives rise to the nucleation of BPDs in 4H-SiC (figures 8(b) and (c)) [82]. Selected area electron diffraction also reveals that the plastic deformation is controlled by the nucleation and slip of BPDs in nanoindented 4H-SiC [86].
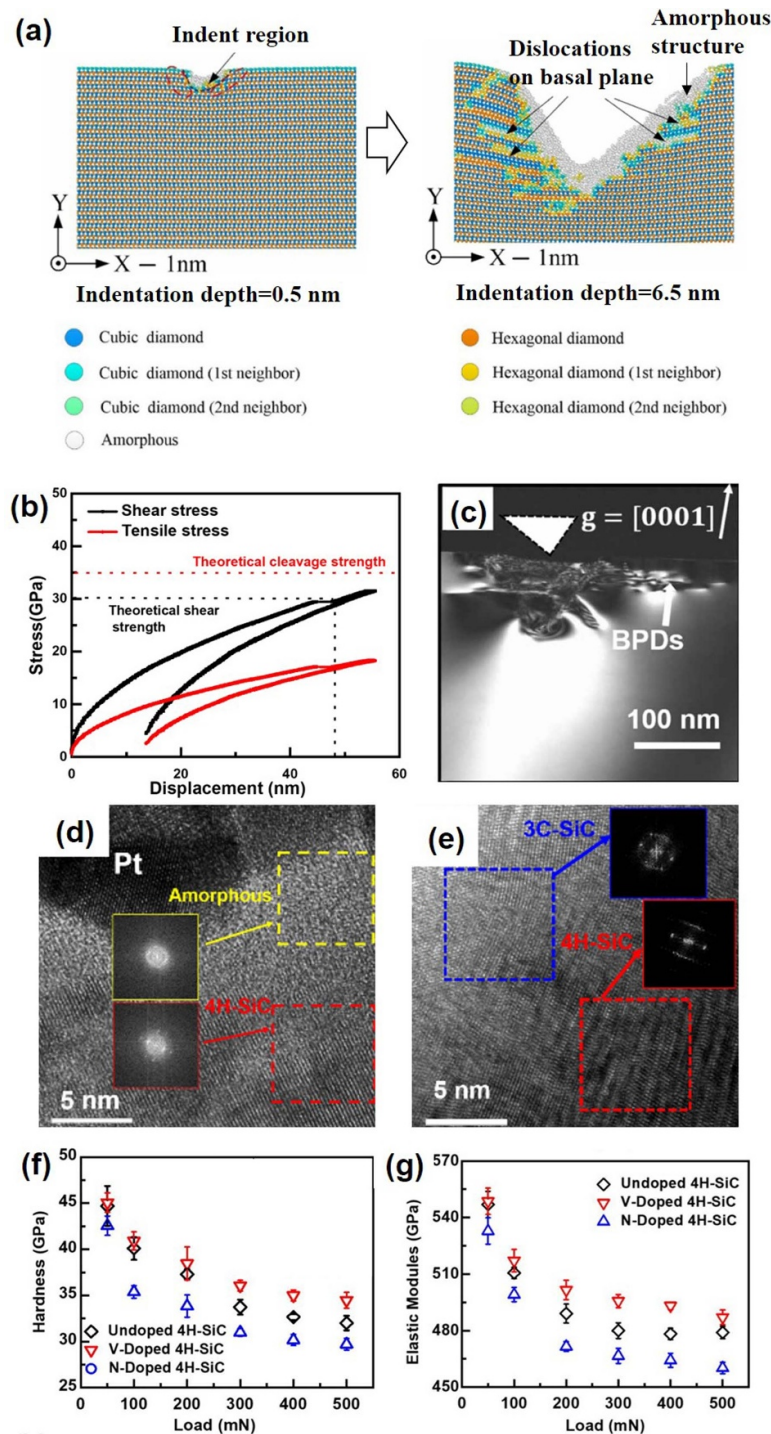
J. Phys. D: Appl. Phys. **55** (2022) 463001

Topical Review

Figure 8. (a) Molecular dynamics simulations showing the three-dimensional deformation models of 4H-SiC with the indentation depth of 0.5 nm and 6.5 nm. Atoms in two kinds of diamond structures, i.e. cubic diamond structure and hexagonal diamond structure, are marked with different colors in the lattice. Reprinted from [81], Copyright (2019), with permission from Elsevier. (b) The calculated stress beneath the indenter as a function of the penetration depth in the nanoindented region of 4H-SiC, which is deduced from one pair of load-displacement curves with one load (upper curve)–unload (lower curve) cycle. (c) Weak-beam dark-field TEM image of the nanoindented 4H-SiC at the pop-in depth, showing the formation of BPDs. $g = [0001]$. The indenter is indicated by the white triangle. (b) and (c) Reproduced from [82]. © IOP Publishing Ltd. All rights reserved. (d) TEM images of the phase transition from crystalline 4H-SiC (red dash line frame) to amorphization (yellow dash line frame) in the subsurface under the indenter, verified with the fast Fourier transform images of corresponded insets. (e) TEM results in the deeper nanoindented region in 4H-SiC. It has transited from 4H phase to 3C phase, which is demonstrated by the fast Fourier transform images of corresponded insets. The average values of (f) hardness and (g) elastic modulus (Young's modulus) for undoped 4H-SiC, V-doped 4H-SiC, and N-doped 4H-SiC. Calculated with the load-displacement curves from the indentation test. The indents on each sample were repeated for eight times with the error bars connecting the maximum and the minimum values. (d)–(g) Reprinted from [84], with the permission of AIP Publishing.

J. Phys. D: Appl. Phys. **55** (2022) 463001

Topical Review

The slip velocity of BPDs linearly increases with the increase of the applied shear stress [83]. As the indentation depth of the indenter or abrasive particles continuously increases, the cross slip of BPDs gives rise to the piling up of BPDs. The accumulated high stress field then leads to the amorphization and phase transition from 4H-SiC to 3C-SiC (figures 8(d) and (e)) [84]. When the indentation depth further increases beyond the critical depth of the plastic-brittle transition, the surface and subsurface cracks appear and material removal happens in 4H-SiC. The critical depth was estimated as 91.7 nm with theoretical result [87].

4.2. Effect of dopants on the deformation of 4H-SiC

The deformation of 4H-SiC is related to the nucleation and slip of BPDs. V doping, N doping, and Al doping are adopted to tune the electronic properties of 4H-SiC to be semi-insulating, *n*-type and *p*-type, respectively [4, 88]. In these cases, the concentrations of the dopants are higher than 10^{18} cm^{-3} in 4H-SiC substrate wafers [88–92]. It is expected that the high concentration of dopants would affect the kinetics of BPDs, and influence the deformation of 4H-SiC. Liu *et al* clarified that N doping weakens the bond strength of 4H-SiC, thus enhancing the nucleation and glide of BPDs in nanoindented N-doped 4H-SiC. In contrast, V doping hinders the glide of BPDs [82]. The accumulation of the stress field facilitates the amorphization and polymorph transition from 4H-SiC to 3C-SiC. With the insights on the effects of dopants on the kinetics of BPDs in 4H-SiC, it was also found that the mechanical properties, such as hardness, elastic modulus, and fracture toughness of 4H-SiC decrease in the order of V doping, undoping and N doping (figures 8(f) and (g)) [84]. The elastic modulus referred to here is Young's modulus. Besides, the slip velocity of dislocations exhibits strong dependence on the injected hole concentration [93]. According to the relationship between the kinetics of BPDs and the mechanical properties of 4H-SiC, it is reasonable to deduce that Al doping might increase the hardness, elastic modulus, and fracture toughness of 4H-SiC.

5. Evolution of dislocations during the homoepitaxy of 4H-SiC

The evolution of dislocations during the homoepitaxy of 4H-SiC is schematically illustrated in figure 9 [6]. During the homoepitaxy of 4H-SiC, more than 95% of TDs in 4H-SiC substrate wafers are inherited to the epitaxial layer [94]. The growth-step-assisted conversion of TSDs to Frank-type SFs is similar to that during the single-crystal growth. TSDs in the substrate act as the nucleation centers of the carrot defects, which consist of two intersecting planar faults on the prismatic plane and the basal plane [95, 96].

The activation barrier for the slip of the Si-core PD comprising a BPD is as low as 0.46 eV [13]. During the application of 4H-SiC bipolar devices, the slip of the Si-core PD comprising the BPD would be activated by the electron–hole recombination, UV illumination or electron
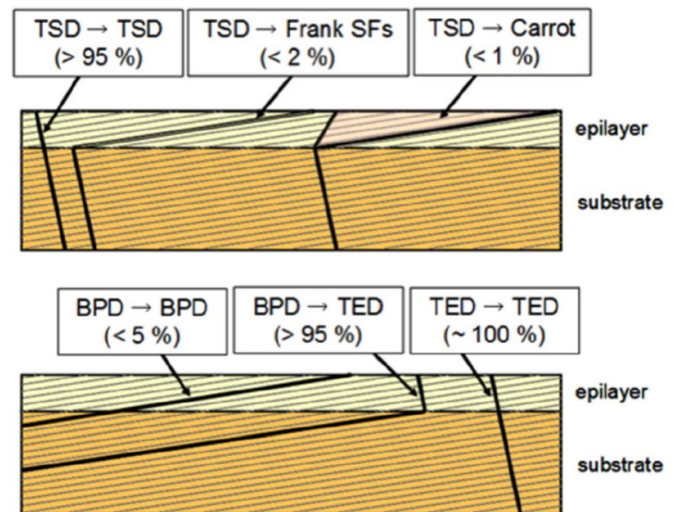

Figure 9. Typical replication and conversion of dislocations in 4H-SiC epi-growth process. Reprinted from [6], with the permission of AIP Publishing.

illumination [97–100], causing the expansion of the Shockley-type SF and the degradation of the reliability of 4H-SiC based bipolar devices. Therefore, various efforts have been dedicated to convert BPDs to TEDs during the homoepitaxy of 4H-SiC, to enhance the reliability of 4H-SiC based bipolar devices. It has been found that increasing the growth rate, inserting a N-doped buffer layer, and high-temperature growth interruptions are beneficial for increasing the conversion ratio of BPDs [101–103]. The pre-growth treatment of 4H-SiC substrates, such as optimizing the cleaning procedure, molten-alkali etching and lithographic patterning, also promotes the conversion of BPDs to TEDs [104–106].

6. Effect of dislocations on the performance of 4H-SiC

6.1. Etch pits of dislocations in 4H-SiC wafers

Molten–alkali etching is one of the most convenient approaches to reveal dislocations and facilitate the statistics of dislocation density in 4H-SiC wafers. The etch pits are formed by removing strained surface atoms surrounding dislocations via preferential etching at the Si-face of 4H-SiC. The preferential etching processes of TEDs and TSDs proceed along the dislocation lines and dislocation steps, which create hexagonal pits at the surface of molten–KOH etched 4H-SiC. The average size of the etch pits of TSDs is about two times larger than that of TEDs [107, 108]. The preferential etching of BPDs in off-axis sliced 4H-SiC starts at the outcrop at the surface, and proceeds along the dislocation line of a BPD, which creates the sea-shell shaped etch pit [109, 110]. In order to increase the shape difference among etch pits of different dislocations, additives, such as NaOH, K_2CO_3, Na_2O_2 and MgO, have been added into molten KOH to facilitate the identification and statistics of different dislocations in 4H-SiC [111–113]. Recently, we proposed to discriminate
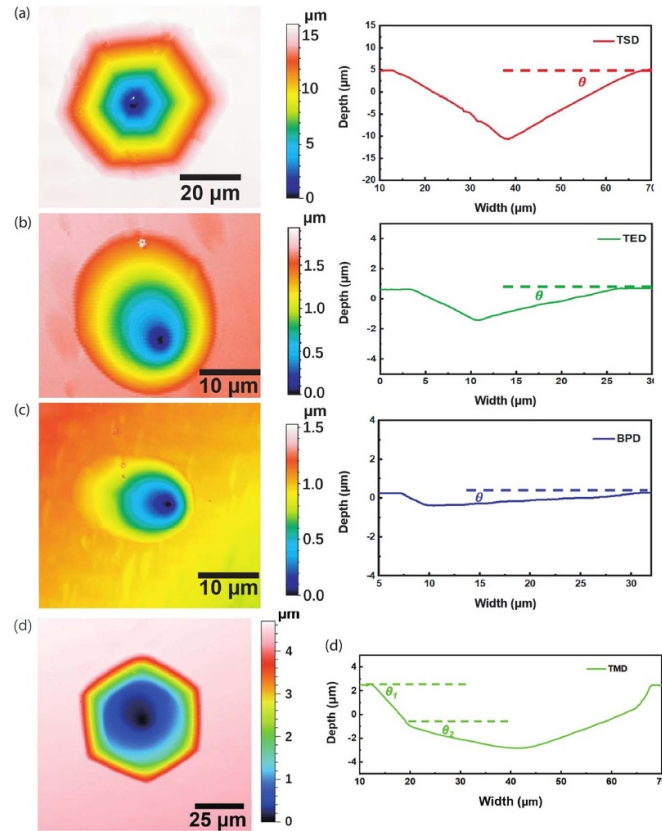
Figure 10. The laser scanning confocal microscope (LSCM) images (left panel) and depth profiles (right panel) of the etch pits of a (a) TSD, (b) TED, (c) BPD and (d) TMD in the molten–KOH etched 4H-SiC. Reproduced from [114]. © 2022 Chinese Institute of Electronics. All rights reserved.

dislocations by the inclination angles for the etch pits of dislocations. In the *n*-type 4H-SiC wafer, the inclination angles for the etch pits of TSDs, TEDs and BPDs are found to be in the range of 27°–35°, 8°–15° and 2°–4°, respectively. In a high-purity semi-insulating 4H-SiC wafer, the inclination angles for the etch pits of TSDs and TEDs are in the range of 31°–34°and 21°–24°, respectively. We also propose to distinguish TMDs from TSDs by the inclination angles, which paves the way for investigations on the properties of TMDs in 4H-SiC (figure 10) [114].

Because the molten-alkali etching rate of the C-face is faster than that of the Si-face of 4H-SiC, the preferential etching from the outcrops of dislocations cannot be triggered during the molten-alkali etching at the C-face of 4H-SiC. The vaporized alkali etching and microwave plasma etching are adopted to reveal dislocations on the C-face of 4H-SiC [115–117].

6.2. Electronic properties of dislocations in 4H-SiC

The local electronic properties of individual dislocations in 4H-SiC have been investigated by combining the molten-alkali etching and the micro-area electrical measurements. Combining molten–KOH etching and the Kelvin probe force microscopy (KPFM), Huang *et al* found that both TEDs and TSDs have lower surface potentials than the dislocation-free region of 4H-SiC epitaxial layer with the N-doping concentration of 1×10^{16} cm^{-3} (figure 11(a)) [118]. Meanwhile, the off-axis electron holography measurements reveal the electrostatic potential distribution of TSDs in 4H-SiC epitaxial layers, which indicates that the dislocation line of a TSD is negatively charged, as shown in figure 11(b) [119]. This result indicates that TSDs create acceptor-like states in the 4H-SiC epitaxial layers with the N-doping concentration of 2.5×10^{16} cm^{-3}. In addition, Luo *et al* found the donor-like states of both TSDs and TEDs in *n*-type 4H-SiC substrates by KPFM results, which can be attributed to the accumulation of nitrogen atoms at the core of TDs, as the N-doping oncentration in *n*-type substrate is 1×10^{18} cm^{-3} [120]. Conductive atomic force microscopy (C-AFM) indicates that the leakage current is enhanced along the dislocation lines of TDs in 4H-SiC, because the leakage current at the bottom of the pit is higher (figure 11(c)) [121]. In addition, surface outcrops of TDs, that is, sharp-apex pits of TSDs and stripe-shaped pits of TEDs, are also found to contribute to the TD-related electrical properties [122]. Tunneling atomic force microscopy results show that the current was highly localized in the sharp-apex pit near its bottom, while it is not distinct at the strip-shaped pits [123]. The defect states of dislocations give rise to electron–hole recombination during the application of 4H-SiC based power devices, which degrades their reliabilities.
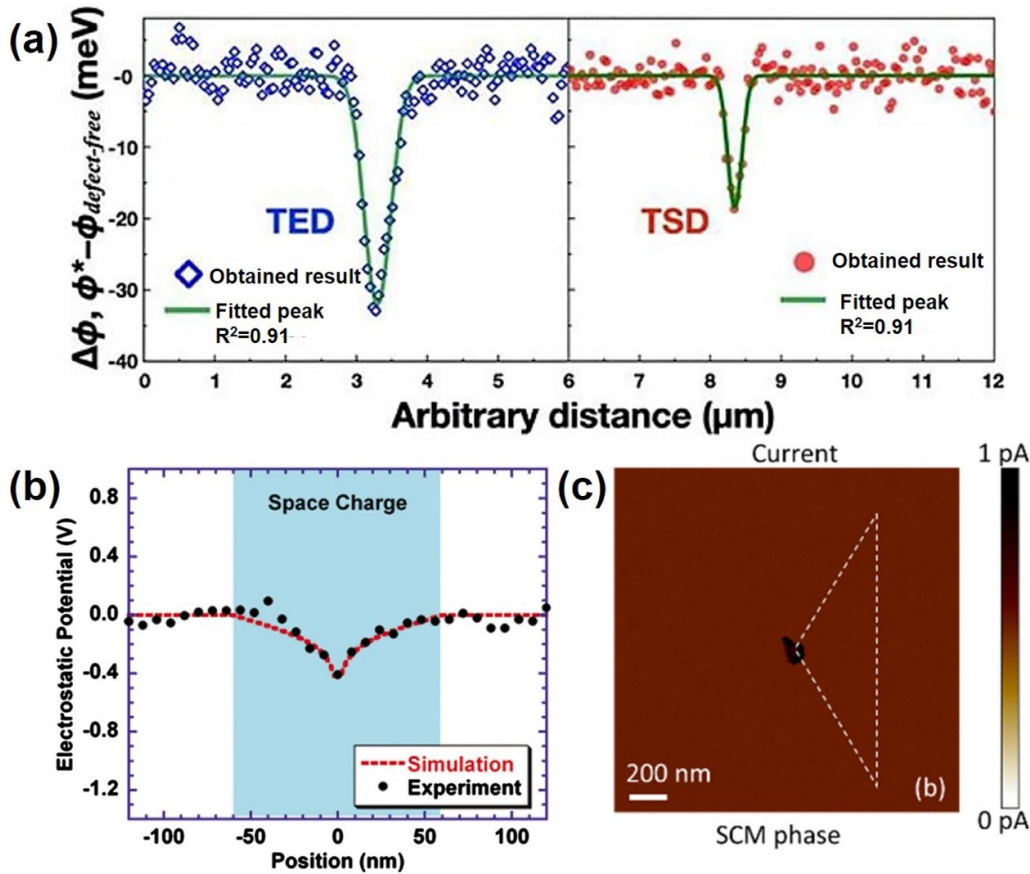
Figure 11. (a) Cross-sectional surface-potentials of molten-alkali etch pits of a TED (left) and a TSD (right) in a 4H-SiC epitaxial layer. Reprinted from [118], Copyright (2022), with permission from Elsevier. (b) The measured (black dots) and simulated (red line) potential line across the dislocation line of the TSD deduced from the electron holography data. Reprinted from [119], with the permission of AIP Publishing. (c) C-AFM current map of a sharp-apex pit. It shows higher current (dark dot) at the bottom of the pit. The other area in the pit marked with dashed triangle is similar with the surrounding area without pits. Reproduced from [121]. © IOP Publishing Ltd. All rights reserved.

It has been found that the TDs lead to the decrease of minority carrier lifetime, increase of the pre-breakdown reverse leakage current, and thus the decrease of the breakdown voltage of 4H-SiC Schottky barrier diodes (SBDs), junction barrier Schottky diodes (JBSDs), p–n junction diodes (PNDs) and avalanche photodiodes (figures 12(a) and (b)) [124–128]. Pits induced by TSDs are found to exert comparable effect on the degradation of 4H-SiC based devices. The effect of TSDs on the degradation of 4H-SiC based devices could be relieved if a TSD does not outcrop at the surface (figure 12(c)), the theoretical results fit the experiments well [129]. BPDs also act as recombination centers in 4H-SiC. In 4H-SiC based bipolar devices, the injection of holes and the subsequent electron–hole recombination give rise to the slip of the Si-core PD, and thus the expansion of the SF comprising a BPD, which significantly degrades the drift conductivity and causes a shift of the forward voltage [10, 11, 130–132]. As figure 12(d) shows, the electron–hole recombination-induced expansion of SFs originates from both the penetrating BPDs and the BPDs segments where the BPD-TED conversion happens, which gives rise to the formation of differently shaped SFs [133].

6.3. Optical properties of dislocations in 4H-SiC

The radiative recombination at dislocations in 4H-SiC gives rise to changes of optical properties of dislocations in 4H-SiC. It is found that the photoluminescence (PL)-intensity contrast of dislocations depends on the minority carrier lifetime. When the minority carrier lifetime is longer than 0.5 μs [134], the contrast of the PL intensity is strong enough to discriminate dislocations, which paves the way for nondestructive analysis of the distribution and density of dislocations both in 4H-SiC wafers and epitaxial layers [135–137]. Figure 13(a)
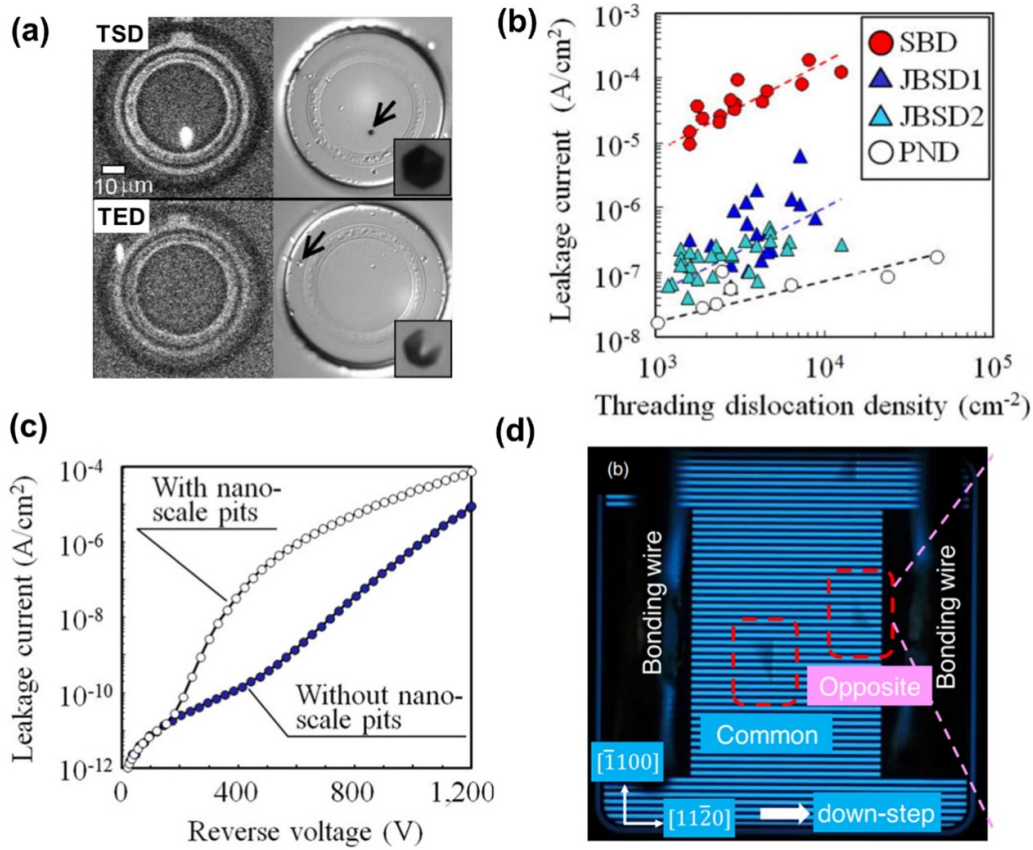
Figure 12. (a) Electroluminescence (EL) images (left panel) and the optical Nomarski contrast images (right panel) after molten–KOH etching of avalanche photodiodes containing a TSD and a TED. The black arrows indicate the positions of the light emission spots. Reprinted from [124], with the permission of AIP Publishing. (b) The leakage-current densities of different 4H-SiC based devices as functions of the density of TDs. Reprinted from [125], with the permission of AIP Publishing. (c) Simulated reverse leakage current curves of a 4H-SiC SBD with and without nanoscale pits. Reprinted from [129], with the permission of AIP Publishing. (d) EL image of a 4H-SiC PiN diode containing two SSFs with opposite expansion direction, observed using a 420 nm band pass filter. Reproduced from [133]. © 2022 The Japan Society of Applied Physics. All rights reserved.

depicts the schematic picture for the recombination path of minority carriers in 4H-SiC [134]. The contrast of dislocations is affected by the lifetime of the minority-carrier of 4H-SiC. For 4H-SiC wafers with the minority-carrier lifetime less than 0.5 μs, most carriers cannot migrate to dislocations, the minority carriers are trapped by intrinsic defects, which yields inconspicuous PL signal of dislocations in the PL-intensity mapping (figure 13(b)). When the minority-carrier lifetime is longer than 0.5 μs, the electron–hole recombination at dislocations results in the strong contrast of dislocations in the PL-intensity mapping (figure 13(c)) [134]. Therefore, PL is one valid nondestructive technique to analyze the distribution and density of dislocations both in 4H-SiC wafers and epitaxial layers. TSDs and TEDs behave as dark or bright spots with different sizes in the PL-intensity-mapping image of the (0001) surface of 4H-SiC; the intrinsic PL emission peaks for TEDs and TSDs locate at 600 nm and 800–850 nm, respectively

[138]. Dislocations in 4H-SiC can also be discriminated by the integration of infrared band emission. With a band-pass filter (900 $\pm$ 5 nm), TSDs, TEDs and BPDs in the infrared PL image of a 4H-SiC epitaxial layer exist as large bright spots, small bright spots, and bright lines, respectively (figure 13(d)) [139]. The PL emission of a BPD originates from the PL emissions of PDs and the SSF comprising the BPD. The PL emission peaks for the Si-core PD, C-core PD and the SSF locate at 670–700 nm, 720–850 nm and 420 nm, respectively [140]. According to the emission wavelength, the single illustration of the PDs and the SSF can be realized. Recently, we found that TDs also contribute to the enhanced D1 luminescence of 4H-SiC (figures 13(e) and (f)) [120], which means that the mapping of the D1 luminescence density would also facilitate the statistics of dislocation density and illustration of the dislocation distribution in 4H-SiC wafers and epitaxial layers.
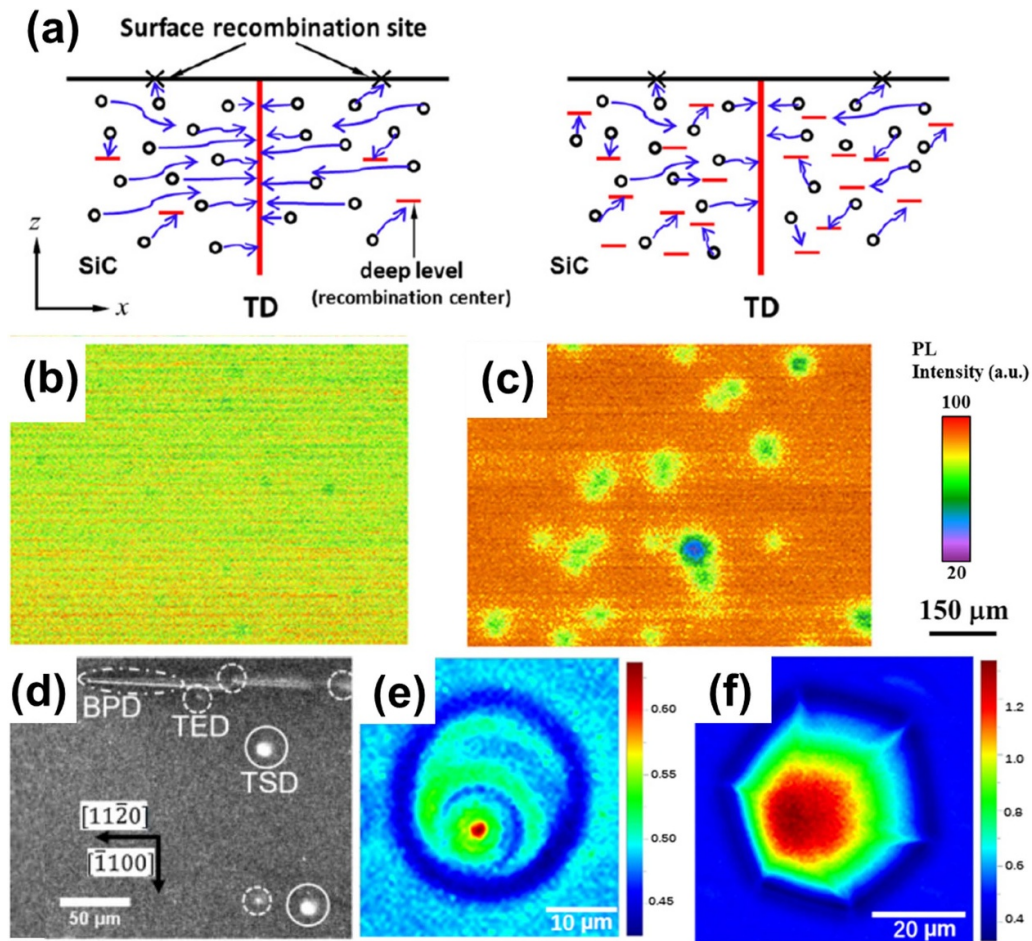
J. Phys. D: Appl. Phys. **55** (2022) 463001

Topical Review

Figure 13. (a) Schematic diagram showing the carrier recombination at TDs in 4H-SiC with long (left) and short (right) minority-carrier lifetime. Micro-PL intensity mapping images taken in 4H-SiC samples with minority-carrier lifetime of (b) 0.1 μs and (c) 1.6 μs with the band-pass filter of 390 nm. (a)–(c) Reprinted from [134], with the permission of AIP Publishing. (d) Micro-PL intensity mapping image of an *n*-type 4H-SiC epitaxial layer taken with a band-pass filter (900 $\pm$ 5 nm). The TSD, TED and BPD are marked. Reprinted from [139], with the permission of IOP Publishing. Micro-PL intensity mapping image of (e) a TED and (f) a TSD in *n*-type 4H-SiC collected for the emission range from 450 nm to 750 nm. (e) and (f) Reprinted with permission from [120]. Copyright (2022) American Chemical Society.

7. Conclusions

As one of the most mature and large-scale developed wide-bandgap semiconductors, 4H-SiC has already flourished in both high-power and high-frequency electronics, and has been successfully applied in electrical vehicles, 5G communications and new-energy systems. The high-density dislocations in 4H-SiC are the most severe bottleneck for advancing the application of 4H-SiC in ultra-high-power electronics. In this topical review, the classification and basic properties of dislocations in 4H-SiC wafers and epitaxial layers have been introduced. The generation, evolution and annihilation of dislocations during the single-crystal growth of 4H-SiC boules, processing of 4H-SiC wafers, as well as homoepitaxy of 4H-SiC layers have been systematically reviewed. Based on the evolution of dislocations, the approaches to reduce the density of dislocations, especially TSDs and BPDs, have been introduced. The characterization and discrimination of dislocations in 4H-SiC are presented. The effect of dislocations on the electronic and optical properties of 4H-SiC wafers and epitaxial layers, as well as the role of dislocations on the device

performance and reliability are finally presented. This topical review provides insight into the fundamentals and evolution of dislocations in 4H-SiC, and is expected to provide inspiration for further control of dislocations in 4H-SiC.

Data availability statement

All data that support the findings of this study are included within the article (and any supplementary files).

Acknowledgments

ORCID iDs

Lingbo Xu ⓘ https://orcid.org/0000-0003-2730-0604
Yiqiang Zhang ⓘ https://orcid.org/0000-0002-2437-925X
Can Cui ⓘ https://orcid.org/0000-0002-8429-5875
Xiaodong Pi ⓘ https://orcid.org/0000-0002-4233-6181
Rong Wang ⓘ https://orcid.org/0000-0003-3333-0180

References

[1] Eddy C R and Gaskill D K 2009 Silicon carbide as a platform for power electronics *Science* **324** 1398–400
[2] Amano H *et al* 2018 The 2018 GaN power electronics roadmap *J. Phys. D: Appl. Phys.* **51** 163001
[3] Lohrmann A, Johnson B C, McCallum J C and Castelletto S 2017 A review on single photon sources in silicon carbide *Rep. Prog. Phys.* **80** 034502
[4] Wellmann P J 2018 Review of SiC crystal growth technology *Semicond. Sci. Technol.* **33** 103001
[5] Manning I, Matsuda Y, Chung G, Sanchez E, Dudley M, Ailihumaer T and Raghothamachar B 2020 Progress in bulk 4H SiC crystal growth for 150 mm wafer production *Mater. Sci. Forum* **1004** 37–43
[6] La Via F, Camarda M and La Magna A 2014 Mechanisms of growth and defect properties of epitaxial SiC *Appl. Phys. Rev.* **1** 031301
[7] Musolino M, Xu X, Wang H, Rengarajan V, Zwieback I, Ruland G, Crippa D, Mauceri M, Calabretta M and Messina A 2021 Paving the way toward the world's first 200mm SiC pilot line *Mater. Sci. Semicond. Process.* **135** 106088
[8] Manning I, Chung G Y, Sanchez E, Dudley M, Ailihumaer T, Guo J Q, Goue O and Raghothamachar B 2019 Influence of dopant concentration on dislocation distributions in 150mm 4H SiC wafers *Mater. Sci. Forum* **963** 60–63
[9] Quast J, Hansen D, Loboda M, Manning I, Moeggenborg K, Mueller S, Parfeniuk C, Sanchez E and Whiteley C 2015 High quality 150 mm 4H SiC wafers for power device production *Mater. Sci. Forum* **821–823** 56–59
[10] Bu Y, Yoshimoto H, Watanabe N and Shima A 2017 Fabrication of 4H-SiC PiN diodes without bipolar degradation by improved device processes *J. Appl. Phys.* **122** 244504
[11] Ota C, Nishio J, Okada A and Iijima R 2021 Origin and generation process of a triangular single Shockley stacking fault expanding from the surface side in 4H-SiC PIN diodes *J. Electron. Mater.* **50** 6504–11
[12] Ishigaki T, Murata T, Kinoshita K, Morikawa T, Oda T, Fujita R, Konishi K, Mori Y and Shima A 2019 Analysis of degradation phenomena in bipolar degradation screening process for SiC-MOSFETs *31st Int. Symp. on Power Semiconductor Devices and ICs (ISPSD)* pp 259–62
[13] Konishi K, Yamamoto S, Nakata S, Nakamura Y, Nakanishi Y, Tanaka T, Mitani Y, Tomita N, Toyoda Y and Yamakawa S 2013 Stacking fault expansion from basal plane dislocations converted into threading edge dislocations in 4H-SiC epilayers under high current stress *J. Appl. Phys.* **114** 014504
[14] Caldwell J D, Stahlbush R E, Ancona M G, Glembocki O J and Hobart K D 2010 On the driving force for recombination-induced stacking fault motion in 4H-SiC *J. Appl. Phys.* **108** 044503
[15] Kimoto T and Watanabe H 2020 Defect engineering in SiC technology for high-voltage power devices *Appl. Phys. Express* **13** 44
[16] Kimoto T and Cooper J A 2014 *Fundamentals of Silicon Carbide Technology: Growth, Characterization, Devices, and Applications* (New York: Wiley)
[17] Hull D and Bacon D J 2011 Defects in crystals *Introduction to Dislocations* (Oxford: Butterworth-Heinemann)
[18] Raghothamachar B, Yang Y, Guo J and Dudley M 2019 Analysis of basal plane dislocation dynamics in PVT-grown 4H-SiC crystals during high temperature treatment *ECS Trans.* **92** 131–9
[19] Chung S, Wheeler V, Myers-Ward R, Eddy C Jr, Gaskill D K, Wu P, Picard Y N and Skowronski M 2011 Direct observation of basal-plane to threading-edge dislocation conversion in 4H-SiC epitaxy *J. Appl. Phys.* **109** 094906
[20] Blumenau A T, Fall C J, Jones R, Öberg S, Frauenheim T and Briddon P R 2003 Structure and motion of basal dislocations in silicon carbide *Phys. Rev. B* **68** 174108
[21] Savini G, Heggie M I, Öberg S and Briddon P R 2007 Electrical activity and migration of 90° partial dislocations in SiC *New J. Phys.* **9** 6
[22] Ishikawa Y, Sudo M, Yao Y-Z, Sugawara Y and Kato M 2018 Expansion of a single Shockley stacking fault in a 4H-SiC (11-20) epitaxial layer caused by electron beam irradiation *J. Appl. Phys.* **123** 225101
[23] Maeda K 2013 Radiation-enhanced dislocation glide: the current status of research *Materials and Reliability Handbook for Semiconductor Optical and Electron Devices* (New York: Springer) pp 263–81
[24] Wellmann P, Neubauer G, Fahlbusch L, Salamon M and Uhlmann N 2015 Growth of SiC bulk crystals for application in power electronic devices-process design, 2D and 3D x-ray *in situ* visualization and advanced doping *Cryst. Res. Technol.* **50** 2–9
[25] Matsumoto M, Huang H, Harada H, Kakimoto K and Yan J 2017 On the phase transformation of single-crystal 4H-SiC during nanoindentation *J. Phys. D: Appl. Phys.* **50** 265303
[26] Shinagawa N, Izawa T, Manabe M, Yamochi T and Ohtani N 2020 Populations and propagation behaviors of pure and mixed threading screw dislocations in physical vapor transport grown 4H-SiC crystals investigated using x-ray topography *Jpn. J. Appl. Phys.* **59** 091002
[27] Hoshino N, Kamata I, Tokuda Y, Makino E, Kanda T, Sugiyama N, Kuno H, Kojima J and Tsuchida H 2017 Fast growth of n-type 4H-SiC bulk crystal by gas-source method *J. Cryst. Growth* **478** 9–16
[28] Suo H, Tsukimoto S, Eto K, Osawa H, Kato T and Okumura H 2018 Evaluation of the increase in threading dislocation during the initial stage of physical vapor transport growth of 4H-SiC *Jpn. J. Appl. Phys.* **57** 065501
[29] Glass R C, Henshall D, Tsvetkov V F and Carter C H 1997 SiC-seeded crystal growth *MRS Bull.* **22** 30–35
[30] Ohtani N, Katsuno M, Tsuge H, Fujimoto T, Nakabayashi M, Yashiro H, Sawamura M, Aigo T and Hoshino T 2006 Dislocation processes during SiC bulk crystal growth *Microelectron. Eng.* **83** 142–5
[31] Sakwe S A and Wellmann P J 2007 Influence of growth temperature on the evolution of dislocations during PVT growth of bulk SiC single crystals *Mater. Sci. Forum* **556–557** 263–6
[32] Sanchez E K, Liu J Q, de Graef M, Skowronski M, Vetter W M and Dudley M 2002 Nucleation of threading dislocations in sublimation grown silicon carbide *J. Appl. Phys.* **91** 1143–8
[33] Dudley M, Huang X R, Huang W, Powell A, Wang S, Neudeck P and Skowronski M 1999 The mechanism of micropipe nucleation at inclusions in silicon carbide *Appl. Phys. Lett.* **75** 784–6

J. Phys. D: Appl. Phys. **55** (2022) 463001

Topical Review

[34] Berkman E *et al* 2009 Defect status in SiC manufacturing *Mater. Sci. Forum* **615–617** 3–6

[35] Leonard R T *et al* 2008 100 mm 4HN-SiC wafers with zero micropipe density *Mater. Sci. Forum* **600–603** 7–10

[36] Nakamura D, Gunjishima I, Yamaguchi S, Ito T, Okamoto A, Kondo H, Onda S and Takatori K 2004 Ultrahigh-quality silicon carbide single crystals *Nature* **430** 1009–12

[37] Sakwe S A, Müller R, Masri P and Wellmann P J 2006 Dislocation evolution and distribution during physical vapor transport (PVT) growth of bulk 6H-SiC single crystals *Phys. Status Solidi* c **3** 562–6

[38] Gao B and Kakimoto K 2014 Dislocation-density-based modeling of the plastic behavior of 4H-SiC single crystals using the Alexander–Haasen model *J. Cryst. Growth* **386** 215–9

[39] Selder M, Kadinski L, Durst F and Hofmann D 2001 Global modeling of the SiC sublimation growth process: prediction of thermoelastic stress and control of growth conditions *J. Cryst. Growth* **226** 501–10

[40] Samant A V, Zhou W L and Pirouz P 1998 Effect of test temperature and strain rate on the yield stress of monocrystalline 6H-SiC *Phys. Status Solidi* a **166** 155–69

[41] Ma R-H, Zhang H, Dudley M and Prasad V 2003 Thermal system design and dislocation reduction for growth of wide band gap crystals: application to SiC growth *J. Cryst. Growth* **258** 318–30

[42] Cherednichenko D I, Drachev R V, Khlebnikov I I, Deng X and Sudarshan T S 2003 Thermal stress as the major factor of defect generation in SiC during PVT growth *MRS Online Proc. Libr.* **742** 218

[43] Zhang M, Hobgood H, Treu M and Pirouz P 2004 Generation of stacking faults in highly doped n-type 4H-SiC substrates *Mater. Sci. Forum* **457–460** 759–62

[44] Maeda K, Suzuki K, Fujita S, Ichihara M and Hyodo S 1988 Defects in plastically deformed 6H SiC single crystals studied by transmission electron microscopy *Phil. Mag.* A **57** 573–92

[45] Suematsu H, Suzuki T, Iseki T and Mori T 1991 Kinking and cracking caused by slip in single crystals of silicon carbide *J. Am. Ceram. Soc.* **74** 173–8

[46] Gao B and Kakimoto K 2014 Three-dimensional modeling of basal plane dislocations in 4H-SiC single crystals grown by the physical vapor transport method *Cryst. Growth Des.* **14** 1272–8

[47] Steiner J, Roder M, Nguyen B D, Sandfeld S, Danilewsky A and Wellmann P J 2019 Analysis of the basal plane dislocation density and thermomechanical stress during 100 mm PVT growth of 4H-SiC *Materials* **12** 2207

[48] Sonoda M, Nakano T, Shioura K, Shinagawa N and Ohtani N 2018 Structural characterization of the growth front of physical vapor transport grown 4H-SiC crystals using x-ray topography *J. Cryst. Growth* **499** 24–29

[49] Nakano T, Shinagawa N, Yabu M and Ohtani N 2019 Formation and multiplication of basal plane dislocations during physical vapor transport growth of 4H-SiC crystals *J. Cryst. Growth* **516** 51–56

[50] Liu J, Gao J, Cheng J, Yang J and Qiao G 2005 Model for micropipe formation in 6H-SiC single crystal by sublimation method *Mater. Lett.* **59** 2374–7

[51] Hofmann D, Schmitt E, Bickermann M, Kölbl M, Wellmann P J and Winnacker A 1999 Analysis on defect generation during the SiC bulk growth process *Mater. Sci. Eng.* B **61–62** 48–53

[52] Heindl J, Dorsch W, Strunk H P, Müller S G, Eckstein R, Hofmann D and Winnacker A 1998 Dislocation content of micropipes in SiC *Phys. Rev. Lett.* **80** 740–1

[53] Maximenko S I, Pirouz P and Sudarshan T S 2006 Open core dislocations and surface energy of SiC *Mater. Sci. Forum* **527–529** 439–42

[54] Mahajan S 2002 Origins of micropipes in SiC crystals *Appl. Phys. Lett.* **80** 4321–3

[55] Lin S, Chen Z, Yang Y, Liu S, Ba Y, Li L and Yang C 2012 Formation and evolution of micropipes in SiC crystals *CrystEngComm* **14** 1588–94

[56] Gutkin M Y, Sheinerman A G, Argunova T S, Je J H, Kang H S, Hwu Y and Tsai W-L 2002 Ramification of micropipes in SiC crystals *J. Appl. Phys.* **92** 889–94

[57] Kojima K, Nishizawa S, Kuroda S, Okumura H and Arai K 2005 Effect of growth condition on micropipe filling of 4H-SiC epitaxial layer *J. Cryst. Growth* **275** e549–54

[58] Kamata I, Tsuchida H, Jikimoto T and Izumi K 2000 Structural transformation of screw dislocations via thick 4H-SiC epitaxial growth *Jpn. J. Appl. Phys.* **39** 6496–500

[59] Shiomi H, Kinoshita H, Furusho T, Hayashi T, Tajima M and Higashi E 2006 Crystal growth of micropipe free 4H-SiC on 4H-SiC {0338} seed and high-purity semi-insulating 6H-SiC *J. Cryst. Growth* **292** 188–91

[60] Xiao S, Harada S, Murayama K, Tagawa M and Ujihara T 2016 Conversion behavior of threading screw dislocations on C face with different surface morphology during 4H-SiC solution growth *Cryst. Growth Des.* **16** 6436–9

[61] Yamamoto Y, Harada S, Seki K, Horio A, Mitsuhashi T, Koike D, Tagawa M and Ujihara T 2014 Low-dislocation-density 4H-SiC crystal growth utilizing dislocation conversion during solution method *Appl. Phys. Express* **7** 065501

[62] Harada S, Yamamoto Y, Seki K, Horio A, Mitsuhashi T, Tagawa M and Ujihara T 2013 Evolution of threading screw dislocation conversion during solution growth of 4H-SiC *APL Mater.* **1** 022109

[63] Yamamoto Y, Harada S, Seki K, Horio A, Mitsuhashi T and Ujihara T 2012 High-efficiency conversion of threading screw dislocations in 4H-SiC by solution growth *Appl. Phys. Express* **5** 115501

[64] Ujihara T, Kozawa S, Seki K, Yamamoto Y and Harada S 2012 Conversion mechanism of threading screw dislocation during SiC solution growth *Mater. Sci. Forum* **717–720** 351–4

[65] Fujimoto T, Ohtani N, Tsuge H, Katsuno M, Sato S, Nakabayashi M and Yano T 2013 A thermodynamic mechanism for PVT growth phenomena of SiC single crystals *ECS J. Solid State Sci. Technol.* **2** N3018–21

[66] Dudley M *et al* 2011 Stacking faults created by the combined deflection of threading dislocations of Burgers vector c and c+a during the physical vapor transport growth of 4H-SiC *Appl. Phys. Lett.* **98** 232110

[67] Wang H *et al* 2014 Characterization of defects in SiC substrates and epilayers *ECS Trans.* **64** 145–52

[68] Mitani T, Eto K, Momose K and Kato T 2021 Massive reduction of threading screw dislocations in 4H-SiC crystals grown by a hybrid method combined with solution growth and physical vapor transport growth on higher off-angle substrates *Appl. Phys. Express* **14** 085506

[69] Chen Y and Dudley M 2007 Direct determination of dislocation sense of closed-core threading screw dislocations using synchrotron white beam x-ray topography in 4H silicon carbide *Appl. Phys. Lett.* **91** 141918

[70] Ohtani N, Katsuno M, Tsuge H, Fujimoto T, Nakabayashi M, Yashiro H, Sawamura M, Aigo T and Hoshino T 2006 Propagation behavior of threading dislocations during physical vapor transport growth of silicon carbide (SiC) single crystals *J. Cryst. Growth* **286** 55–60

[71] Harada S, Yamamoto Y, Seki K, Horio A, Tagawa M and Ujihara T 2014 Different behavior of threading edge dislocation conversion during the solution growth of 4H-SiC depending on the Burgers vector *Acta Mater.* **81** 284–90

J. Phys. D: Appl. Phys. **55** (2022) 463001

Topical Review

[72] Nakamura D, Yamaguchi S, Gunjishima I, Hirose Y and Kimoto T 2007 Topographic study of dislocation structure in hexagonal SiC single crystals with low dislocation density *J. Cryst. Growth* **304** 57–63

[73] Yao Y-Z, Ishikawa Y, Sugawara Y, Saitoh H, Danno K, Suzuki H, Kawai Y and Shibata N 2011 Molten KOH etching with Na_2O_2 additive for dislocation revelation in 4H-SiC epilayers and substrates *Jpn. J. Appl. Phys.* **50** 075502

[74] Sun W, Song Y, Liu C, Peng T, Wang W and Chen X 2015 Basal plane dislocation-threading edge dislocation complex dislocations in 6H-SiC single crystals *Mater. Express* **5** 63–67

[75] Wang H *et al* 2012 Basal plane dislocation multiplication via the Hopping Frank-Read source mechanism in 4H-SiC *Appl. Phys. Lett.* **100** 172105

[76] Deng H, Liu N, Endo K and Yamamura K 2018 Atomic-scale finishing of carbon face of single crystal SiC by combination of thermal oxidation pretreatment and slurry polishing *Appl. Surf. Sci.* **434** 40–48

[77] He Y, Yuan Z, Song S, Gao X and Deng W 2021 Investigation on material removal mechanisms in photocatalysis-assisted chemical mechanical polishing of 4H-SiC wafers *Int. J. Precis. Eng. Manuf.* **22** 951–63

[78] Meng B, Zhang F and Li Z 2015 Deformation and removal characteristics in nanoscratching of 6H-SiC with Berkovich indenter *Mater. Sci. Semicond. Process.* **31** 160–5

[79] Goel S, Yan J, Luo X and Agrawal A 2014 Incipient plasticity in 4H-SiC during quasistatic nanoindentation *J. Mech. Behav. Biomed. Mater.* **34** 330–7

[80] Prasad K E and Ramesh K T 2019 Hardness and mechanical anisotropy of hexagonal SiC single crystal polytypes *J. Alloys Compd.* **770** 158–65

[81] Zhu B, Zhao D and Zhao H 2019 A study of deformation behavior and phase transformation in 4H-SiC during nanoindentation process via molecular dynamics simulation *Ceram. Int.* **45** 5150–7

[82] Liu X, Wang R, Zhang J, Lu Y, Zhang Y, Yang D and Pi X 2022 Doping-dependent nucleation of basal plane dislocations in 4H-SiC *J. Phys. D: Appl. Phys.* **55** 334002

[83] Idrissi H, Lancin M, Regula G and Pichaud B 2004 Study of dislocation mobility in 4H SiC by X-ray transmission topography, chemical etching and transmission electron microscopy *Mater. Sci. Forum* **457–460** 355–8

[84] Liu X, Zhang J, Xu B, Lu Y, Zhang Y, Wang R, Yang D and Pi X 2022 Deformation of 4H-SiC: the role of dopants *Appl. Phys. Lett.* **120** 052105

[85] Nawaz A, Mao W G, Lu C and Shen Y G 2017 Nano-scale elastic-plastic properties and indentation-induced deformation of single crystal 4H-SiC *J. Mech. Behav. Biomed. Mater.* **66** 172–80

[86] Yan J, Gai X and Harada H 2010 Subsurface damage of single crystalline silicon carbide in nanoindentation tests *J. Nanosci. Nanotechnol.* **10** 7808–11

[87] Chai P, Li S and Li Y 2019 Modeling and experiment of the critical depth of cut at the ductile–brittle transition for a 4H-SiC single crystal *Micromachines* **10** 282

[88] Huang Y, Wang R, Qian Y, Zhang Y, Yang D and Pi X 2022 Theoretical study on the improvement of the doping efficiency of Al in 4H-SiC by co-doping group-IVB elements *Chin. Phys. B* **31** 046104

[89] Reshanov S A 2000 Growth and high temperature performance of semi-insulating silicon carbide *Diam. Relat. Mater.* **9** 480–2

[90] Onoue K, Nishikawa T, Katsuno M, Ohtani N, Yashiro H and Kanaya M 1996 Nitrogen incorporation kinetics during the sublimation growth of 6H and 4H SiC *Jpn. J. Appl. Phys.* **35** 2240–3

[91] Ji S, Kojima K, Ishida Y, Saito S, Kato T, Tsuchida H, Yoshida S and Okumura H 2013 The growth of low resistivity, heavily Al-doped 4H-SiC thick epilayers by hot-wall chemical vapor deposition *J. Cryst. Growth* **380** 85–92

[92] Kimoto T 2016 Bulk and epitaxial growth of silicon carbide *Prog. Cryst. Growth Charact. Mater.* **62** 329–51

[93] Tawara T *et al* 2018 Injected carrier concentration dependence of the expansion of single Shockley-type stacking faults in 4H-SiC PiN diodes *J. Appl. Phys.* **123** 025707

[94] Ellison A, Sörman E, Sundqvist B, Magnusson B, Yang Y, Guo J Q, Goue O, Raghothamachar B and Dudley M 2016 Mapping of threading screw dislocations in 4H n-type SiC wafers *Mater. Sci. Forum* **858** 376–9

[95] Benamara M, Zhang X, Skowronski M, Ruterana P, Nouet G, Sumakeris J J, Paisley M J and O'Loughlin M J 2005 Structure of the carrot defect in 4H-SiC epitaxial layers *Appl. Phys. Lett.* **86** 021905

[96] Kimoto T, Miyamoto N and Matsunami H 1999 Performance limiting surface defects in SiC epitaxial p-n junction diodes *IEEE Trans. Electron Devices* **46** 471–7

[97] Yamashita Y, Nakata R, Nishikawa T, Hada M and Hayashi Y 2018 Expansion of Shockley stacking fault observed by scanning electron microscope and partial dislocation motion in 4H-SiC *J. Appl. Phys.* **123** 161580

[98] Yakimov E E and Yakimov E B 2020 Radiation-enhanced dislocation glide in 4H-SiC at low temperatures *J. Alloys Compd.* **837** 155470

[99] Galeckas A, Linnros J and Pirouz P 2006 Recombination-induced stacking faults: evidence for a general mechanism in hexagonal SiC *Phys. Rev. Lett.* **96** 025502

[100] Caldwell J D, Glembocki O J, Stahlbush R E and Hobart K D 2007 Influence of temperature on Shockley stacking fault expansion and contraction in SiC PiN diodes *J. Electron. Mater.* **37** 699–705

[101] VanMil B L, Stahlbush R E, Myers-Ward R L, Lew K-K, Jr E C and Gaskill D K 2008 Basal plane dislocation reduction for 8° off-cut, 4H-SiC using *in situ* variable temperature growth interruptions *J. Vac. Sci. Technol. B* **26** 1504–7

[102] Hori T, Danno K and Kimoto T 2007 Fast homoepitaxial growth of 4H-SiC with low basal-plane dislocation density and low trap concentration by hot-wall chemical vapor deposition *J. Cryst. Growth* **306** 297–302

[103] Balachandran A, Sudarshan T S and Chandrashekhar M V S 2017 Basal plane dislocation free recombination layers on low-doped buffer layer for power devices *Cryst. Growth Des.* **17** 1550–7

[104] Sumakeris J *et al* 2006 Techniques for minimizing the basal plane dislocation fensity in SiC epilayers to reduce V_f drift in SiC bipolar power devices *Mater. Sci. Forum* **527** 141–6

[105] Zhang Z, Moulton E and Sudarshan T S 2006 Mechanism of eliminating basal plane dislocations in SiC thin films by epitaxy on an etched substrate *Appl. Phys. Lett.* **89** 081910

[106] Baierhofer D, Thomas B, Staiger F, Marchetti B, Förster C and Erlbacher T 2022 Defect reduction in SiC epilayers by different substrate cleaning methods *Mater. Sci. Semicond. Process.* **140** 106414

[107] Dong L, Zheng L, Liu X F, Zhang F, Yan G G, Li X G, Sun G S and Wang Z G 2013 Defect revelation and evaluation of 4H silicon carbide by optimized molten KOH etching method *Mater. Sci. Forum* **740–742** 243–6

[108] Liu X F *et al* 2020 Defect appearance on 4H-SiC homoepitaxial layers via molten KOH etching *J. Cryst. Growth* **531** 125359

[109] Nishio J, Ota C, Okada A and Iijima R 2020 Informative aspects of molten KOH etch pits formed at basal plane

J. Phys. D: Appl. Phys. **55** (2022) 463001

Topical Review

dislocations on the surface of 4H-SiC *Phys. Status Solidi* a
217 2000332

[110] Zhuang D and Edgar J H 2005 Wet etching of GaN, AlN, and
SiC: a review *Mater. Sci. Eng. R Rep.* **48** 1–46

[111] Katsuno M, Ohtani N, Takahashi J, Yashiro H and Kanaya M
1999 Mechanism of molten KOH etching of SiC single
crystals: comparative study with thermal oxidation *Jpn. J.
Appl. Phys.* **38** 4661–5

[112] Pal P, Kumar S and Singh S K 2020 Study of eutectic etching
process for defects analysis in n type 4H SiC *Def. Sci. J.*
70 515–9

[113] Song H, Rana T and Sudarshan T S 2011 Investigations of
defect evolution and basal plane dislocation elimination in
CVD epitaxial growth of silicon carbide on eutectic etched
epilayers *J. Cryst. Growth* **320** 95–102

[114] Yang G *et al* 2022 Discrimination of dislocations in 4H-SiC
by inclination angles of molten-alkali etched pits
J. Semicond. **43** 1–7

[115] Yao Y-Z, Ishikawa Y, Sato K, Sugawara Y, Danno K,
Suzuki H and Bessho T 2012 Dislocation revelation
from (0001) carbon-face of 4H-SiC by using
vaporized KOH at high temperature *Appl. Phys. Express*
5 075601

[116] Yu J, Yang X, Peng Y, Hu X, Wang X, Chen X and Xu X
2021 Revelation of the dislocations in the C-face of
4H-SiC substrates using a microwave plasma etching
treatment *CrystEngComm* **23** 353–9

[117] Yao Y Z, Ishikawa Y, Sato K, Sugawara Y, Danno K,
Suzuki H and Bessho T 2013 Large-area mapping of
dislocations in 4H-SiC from carbon-face (000–1) by using
vaporized KOH etching near 1000 °C *Mater. Sci. Forum*
740–742 829–32

[118] Huang J-R, Chen T-W, Lee J-W, Huang C-F and Hong L-S
2022 A perspective on leakage current induced by
threading dislocations in 4H-SiC Schottky barrier diodes
Mater. Lett. **310** 131506

[119] Chung S, Berechman R A, McCartney M R and
Skowronski M 2011 Electronic structure analysis of
threading screw dislocations in 4H-SiC using electron
holography *J. Appl. Phys.* **109** 034906

[120] Luo H, Li J, Yang G, Zhu R, Zhang Y, Wang R, Yang D and
Pi X 2022 Electronic and optical properties of threading
dislocations in n-type 4H-SiC *ACS Appl. Electron. Mater.*
4 1678–83

[121] Fiorenza P, Alessandrino M S, Carbone B, di Martino C,
Russo A, Saggio M, Venuto C, Zanetti E, Giannazzo F and
Roccaforte F 2020 Understanding the role of threading
dislocations on 4H-SiC MOSFET breakdown under high
temperature reverse bias stress *Nanotechnology*
31 125203

[122] Picard Y N, Liu K X, Stahlbush R E and Twigg M E 2008
Imaging surface pits and dislocations in 4H-SiC by
forescattered electron detection and photoluminescence
J. Electron. Mater. **37** 655–61

[123] Ohtani N, Ushio S, Kaneko T, Aigo T, Katsuno M,
Fujimoto T and Ohashi W 2012 Tunneling atomic force
microscopy studies on surface growth pits due to
dislocations in 4H-SiC epitaxial layers *J. Electron. Mater.*
41 2193–6

[124] Berechman R A, Skowronski M, Soloviev S and Sandvik P
2010 Electrical characterization of 4H-SiC avalanche
photodiodes containing threading edge and screw
dislocations *J. Appl. Phys.* **107** 114504

[125] Fujiwara H, Naruoka H, Konishi M, Hamada K, Katsuno T,
Ishikawa T, Watanabe Y and Endo T 2012 Relationship
between threading dislocation and leakage current in
4H-SiC diodes *Appl. Phys. Lett.* **100** 242102

[126] Chynoweth A G and Pearson G L 1958 Effect of dislocations
on breakdown in silicon p-n junctions *J. Appl. Phys.*
29 1103–10

[127] Neudeck P G, Wei H and Dudley M 1999 Study of bulk
and elementary screw dislocation assisted reverse
breakdown in low-voltage (<250 V) 4H-SiC p$^+$n junction
diodes part I: DC properties *IEEE Trans. Electron Devices*
46 478–84

[128] Neudeck P G, Huang W and Dudley M 1998 Breakdown
degradation associated with elementary screw dislocations
in 4H-SiC p$^+$n junction rectifiers *Solid State Electron.*
42 2157–64

[129] Fujiwara H, Naruoka H, Konishi M, Hamada K, Katsuno T,
Ishikawa T, Watanabe Y and Endo T 2012 Impact of
surface morphology above threading dislocations on
leakage current in 4H-SiC diodes *Appl. Phys. Lett.*
101 042104

[130] Skowronski M and Ha S 2006 Degradation of hexagonal
silicon-carbide-based bipolar devices *J. Appl. Phys.*
99 011101

[131] Skowronski M, Liu J Q, Vetter W M, Dudley M, Hallin C
and Lendenmann H 2002 Recombination-enhanced defect
motion in forward-biased 4H-SiC p-n diodes *J. Appl.
Phys.* **92** 4699–704

[132] Twigg M E, Stahlbush R E, Fatemi M, Arthur S D,
Fedison J B, Tucker J B and Wang S 2003 Structure of
stacking faults formed during the forward bias of 4H-SiC
p-i-n diodes *Appl. Phys. Lett.* **82** 2410–2

[133] Nishio J, Ota C and Iijima R 2022 Structural study of single
Shockley stacking faults terminated near substrate/epilayer
interface in 4H-SiC *Jpn. J. Appl. Phys.* **61** SC1005

[134] Feng G, Suda J and Kimoto T 2011 Nonradiative
recombination at threading dislocations in 4H-SiC
epilayers studied by micro-photoluminescence mapping
J. Appl. Phys. **110** 033525

[135] Berwian P, Kaminzky D, Roßhirt K, Kallinger B, Friedrich J,
Oppel S, Schneider A and Schütz M 2015 Imaging defect
luminescence of 4H-SiC by ultraviolet-photoluminescence
Solid State Phenom. **242** 484–9

[136] Stahlbush R E, Liu K X, Zhang Q and Sumakeris J J 2007
Whole-wafer mapping of dislocations in 4H-SiC epitaxy
Mater. Sci. Forum **556–557** 295–8

[137] Tanuma R, Kamata I, Hadorn J P and Tsuchida H 2018
Two-photon-excited, three-dimensional
photoluminescence imaging and dislocation-line analysis
of threading dislocations in 4H-SiC *J. Appl. Phys.*
124 125703

[138] Liu K X, Zhang X, Stahlbush R E, Skowronski M and
Caldwell J D 2008 Differences in emission spectra of
dislocations in 4H-SiC epitaxial layers *Mater. Sci. Forum*
600–603 345–8

[139] Kawahara C, Suda J and Kimoto T 2014 Identification of
dislocations in 4H-SiC epitaxial layers and substrates
using photoluminescence imaging *Jpn. J. Appl. Phys.*
53 020304

[140] Nishio J, Okada A, Ota C and Kushibe M 2020
Photoluminescence analysis of individual partial
dislocations in 4H-SiC epilayers *Mater. Sci. Forum*
1004 376–86